Chemical Engineering Journal 495 (2024) 153368

Contents lists available at ScienceDirect

Chemical Engineering Journal

journal homepage: www.elsevier.com/locate/cej

# Harnessing bimetallic iMWA nanosensitizer to unleash ferroptosis and calcium overload: Unlocking tumor vulnerability for potentiated iMWA therapy against hepatocellular carcinoma

Guanhua Qiu [a,1], Duo Wang [a,c,1,*], Peihan Xie [a,1], Zelun Li [a,d], Niqiang Zhou [a,d], Xiaoqian Zhang [a,d], Xiaobo Wang [a], Jiali Tang [a], Jun Cao [b], Junjie Liu [a,**], Danke Su [a,**]

[a] Department of Radiology, Department of Ultrasound, Department of Hepatobiliary Surgery, Guangxi Medical University Cancer Hospital, Guangxi Medical University, Nanning 530021, Guangxi, PR China
[b] National Engineering Research Center for Biomaterials, Sichuan University, 610064 Chengdu, PR China
[c] Center of Interventional Radiology & Vascular Surgery, Department of Radiology, Zhongda Hospital, Medical School, Southeast University, Nanjing 224001, PR China
[d] Guangxi Key Laboratory of Early Prevention and Treatment for Regional High Frequency Tumor, Nanning 530021, Guangxi, PR China

ARTICLE INFO

*Keywords:*
Bimetallic nanosensitizer
Hepatocellular carcinoma
Microwave ablation
Ferroptosis
Calcium overload
Metal-coordination interactions

ABSTRACT

Microwave ablation (MWA) holds promise as a tumor treatment modality, yet incomplete ablation with low-frequency MWA (iMWA) remains a significant obstacle to survival, while the high-frequency MWA poses safety concerns. To address these challenges, we introduce a novel bimetallic iMWA nanosensitizer, CFT-NPs, constructed via metal-coordination interactions between tannic acid (TA) and iron/calcium dual metal ions ($Fe^{3+}$/$Ca^{2+}$). The $Fe^{3+}$/$Ca^{2+}$ in CFT-NPs work in harmony to convert electromagnetic energy into heat, thereby bolstering the effectiveness of iMWA while maintaining good biosafety. Furthermore, the pH-triggered rupture of CFT-NPs release TA, $Fe^{3+}$, and $Ca^{2+}$. The liberated $Fe^{3+}$ undergoes reduction by TA, and when combined with $Ca^{2+}$, they trigger ferroptosis and $Ca^{2+}$ overload respectively, significantly amplifying the therapeutic effects of iMWA. Utilization iMWA with CFT-NPs results in lipid oxidation, mitochondrial dysfunction, and disruption of redox balance, both *in vitro* and *in vivo*. Notably, this nanosensitizer exerts a robust antitumor effect, effectively inhibiting tumor growth and downregulating the expression of matrix metalloproteinases, which is associated with tumor metastasis. Collectively, this innovative study offers a promising approach to overcome the challenges of incomplete ablation and biological safety, enhancing the antitumor efficacy of iMWA..

## 1. Introduction

Microwave ablation (MWA), a minimally invasive interventional treatment for solid tumors, is particularly favored for the local, minimally invasive management of hepatocellular carcinoma (HCC), which comprises a significant majority of primary liver cancers, estimated to account for roughly 90 % of cases. Its advantages over surgical methods include deep tissue penetration, a shorter treatment cycle, and minimal side effects, making it a highly effective option for treating HCC [1–4]. The mechanism of MWA refers to the absorption of microwave electromagnetic energy by the tumor tissue and its conversion into heat energy, ultimately inducing coagulation necrosis of tumor cells [5]. But MWA also suffers from low energy conversion efficiency from MW electromagnetic energy to heat energy, this occurrence causes the thermal field of the MWA to fail to cover the tumour lesion, resulting in incomplete ablation and non-fatal thermal injury to the tumour. This will further change residual tumour cells into aggressive cells leading to unsatisfactory MWA results such as recurrence and metastasis, especially for large tumors or irregular tumors and tumors in high-risk sites such as early small cell hepatocellular carcinoma [6–8]. Although increasing the power of MWA and prolonging the ablation time can enhance the therapeutic effect on tumors, it also brings biological safety

* Corresponding author at: Department of Radiology, Department of Ultrasound, Department of Hepatobiliary Surgery, Guangxi Medical University Cancer Hospital, Guangxi Medical University, Nanning 530021, Guangxi, PR China.
** Corresponding authors.
*E-mail addresses:* wangduo2022@126.com (D. Wang), liujunjie@gxmu.edu.cn (J. Liu), sudanke33@sina.com (D. Su).
[1] These authors contributed equally to this work.

https://doi.org/10.1016/j.cej.2024.153368
Received 31 March 2024; Received in revised form 18 May 2024; Accepted 20 June 2024
Available online 21 June 2024

issues associated with high power, such as severe thermal damage to surrounding healthy tissues and side effects such as ablation sequelae and bilious pleuritis [9]. Therefore, strategies for enhancing microwave energy conversion efficiency, increasing the efficiency of tumor ablation, and ensuring biological safety are urgently needed to enhance iMWA's anti-tumor effect [10].

In recent years, the concept of utilizing metal ions to continuously reorient under oscillating electromagnetic radiation in order to enhance the conversion efficiency of microwave energy into thermal energy has received widespread attention [11,12]. Compared to traditional ionic solutions, encapsulating metal ions within nanometer or micrometer-scale structures allows for the exhibition of strong non-elastic collision characteristics due to spatial confinement effects, which significantly improves the conversion efficiency of microwave energy [13]. Additionally, these nanometer-scale properties enable metal ions to selectively accumulate at tumor sites, reducing thermal damage to normal tissues and potential ionic toxicity [14–16]. Beyond enhancing heat conversion efficiency, metal ions possess the ability to disrupt intracellular ion homeostasis. For instance, iron or calcium ions ($Fe^{2+}$ or $Ca^{2+}$) can induce ferroptosis or calcium overload, leading to cell apoptosis [17–19]. When combined with iMWA, this capability further enhances tumor suppression [19]. Notably, certain metal ions such as $Ca^{2+}$ can also enhance the thermal conduction efficiency of iMWA, thereby improving the utilization of MWA heat [20–22]. Given the impact of different metal ions on microwave energy conversion efficiency and intracellular ion homeostasis, the development of multi-metal ion-based iMWA sensitizers has emerged as a research focus for future studies [23]. Through meticulous design, different metal ions can act synergistically to enhance microwave energy conversion efficiency while also disrupting tumor intracellular ion homeostasis through multiple avenues, ultimately inhibiting tumor growth [24].

Based on this, we have developed a bimetallic iMWA nanosensitizer aimed at enhancing the conversion efficiency of electromagnetic energy into heat energy (i.e., temperature) and increasing MWA sensitivity by inducing multiple cell death pathways within tumor cells through the destruction of intracellular ion homeostasis by dual metal ions. Utilizing the reducing property of TA as the organic ligand and $Fe^{2+}$ and $Ca^{2+}$ capable of inducing ferroptosis and calcium overload as metal ions, a bimetallic nanocarrier was constructed through metal coordination interactions [25–29]. This nanosensitizer presented the ability to accumulate at the tumor site via enhanced permeability and retention (EPR) effects [30]. Upon internalization, the dual metal ions in the nanosensitizer enhanced the conversion of microwave energy into heat due to their confinement effect. Subsequently, the acidic environment within tumor cells promoted the release of $Fe^{3+}$ and $Ca^{2+}$. The released $Fe^{3+}$ was reduced to $Fe^{2+}$ by TA, consuming intracellular $H_2O_2$ to generate hydroxyl radicals (•OH), which further induced lipid peroxidation (LPO) deposition and oxidative stress imbalance such as glutathione (GSH) depletion, promoting tumor ferroptosis [31,32]. Simultaneously, released $Ca^{2+}$ accumulated in mitochondria, leading to mitochondrial oxidative stress, mitochondrial damage, ATP synthesis reduction, and $Ca^{2+}$ pump ATP2B4 interruption [27,33]. This process further promoted reactive oxygen species (ROS) production, enhanced Calpain-1 expression, and activated the caspase apoptotic pathway triggered by mitochondrial damage [34,35]. In vivo and *in vitro* results demonstrated that the nanosensitizer significantly inhibited tumor growth through dual-metal ion-sensitized iMWA combined with ferroptosis and calcium overload, along with good biocompatibility. It also reduced the expression of matrix metalloproteinases (MMP 2 and MMP 9) which would promote tumor metastasis [36,37]. In all, the constructed bimetallic iMWA nanosensitizer has the potential to address incomplete MWA challenges through the combination effects of enhanced energy conversion efficiency and metal ions-induced cell death, providing a new direction for iMWA nanosensitizer design (Scheme 1).

## 2. Material and methods

### 2.1. Materials

Anhydrous calcium chloride and tannic acid (TA) were purchased from Aladdin Reagent Co., Ltd (Shanghai, China). Ferric chloride hexahydrate was sourced from Leyan (Shanghai, China). The calcium

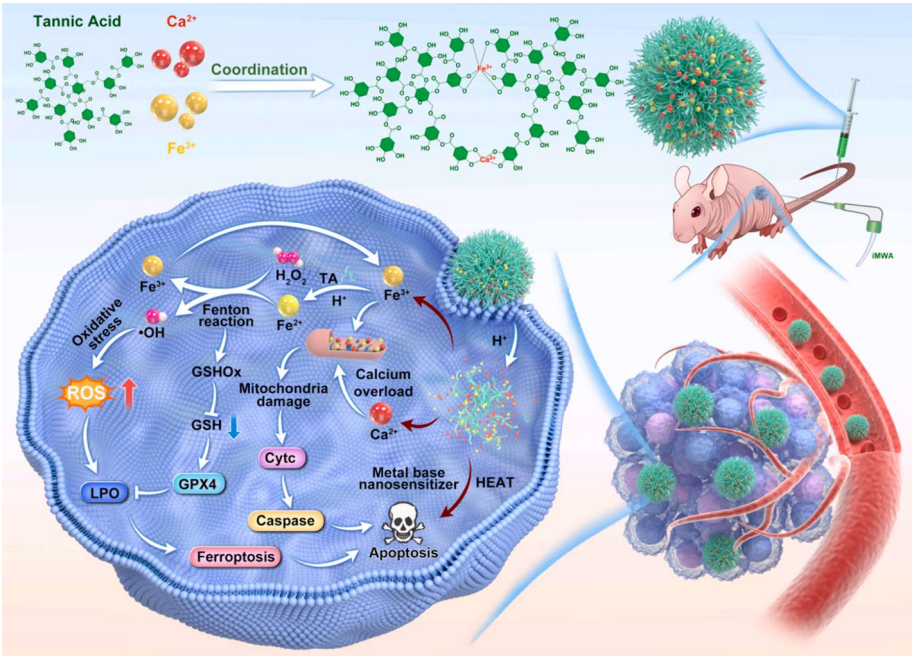


**Scheme 1. A scheme illustrating the mechanism of CFT-NPs bimetallic MWA nanosensitizers in enhancing MWA treatment and boosting antitumor activity.** The CFT-NPs bimetallic MWA nanosensitizer can be used as a microwave heating sensitizer to enhance the MWA of tumors. Meanwhile, the presence of excessive $Ca^{2+}$ and $Fe^{2+}$ can further promote tumor MWA by disrupting intracellular calcium homeostasis, inducing ferroptosis, and damaging mitochondria in the tumor microenvironment.

colorimetric assay kit was obtained from Beyotime Biotechnology (Shanghai, China). All chemicals were of analytical grade and used without further purification. Confocal culture dishes were acquired from Nestle Biotechnology Co., Ltd (Shanghai, China). DMEM medium, trypsin-EDTA solution, and penicillin–streptomycin liquid (penicillin: 10,000 U/mL, streptomycin: 10 mg/mL) were acquired from Solarbio Science & Technology Co., Ltd (Beijing, China). Fetal bovine serum (FBS) was sourced from Wisent Biotechnology Co., LTD (Nanjing, China). Cy5.5 was purchased from Sigma Aldrich Trading Co., LTD (Shanghai, China). The Annexin V-FITC apoptosis detection kit, calcein AM/PI assay kit, DCFH-DA probes, mitochondrial membrane potential assay kit with JC-1, RIPA lysis buffer, bicinchoninic acid (BCA) protein assay kit, western blot (WB) transfer buffer, QuickBlock™ blocking buffer for western blot, and horseradish peroxidase (HRP)-labeled goat anti-rabbit IgG(H + L) were obtained from Beyotime Biotechnology Inc (Shanghai, China). The PAGE gel rapid preparation kit (12.5 %) was obtained from Epizyme Biomedical Technology Co., Ltd (Shanghai, China). Hoechst 33,342 was sourced from Solarbio Science & Technology Co., Ltd (Beijing, China). Thiol tracker violet dye and Image-iT™ lipid peroxidation kit were purchased from Invitrogen (Shanghai, China). The Ferro-Orange staining fluorescent probe was procured from Dojindo Chemical Research Institute (Japan). The fluorescent markers Ca-F07 and M11 mitochondrial staining fluorescent probes were acquired from Bestbio Biotechnology Co., LTD (Nanjing, China). The Caspase 3 rabbit polyclonal antibody (A16793), Caspase 9 rabbit polyclonal antibody (A0281), Calpain-1 rabbit monoclonal antibody (A8710), ATP2B4 rabbit polyclonal antibody (A10105), MMP 9 rabbit monoclonal antibody (A23919), MMP 2 rabbit monoclonal antibody (A19080), GPX 4 rabbit polyclonal antibody (A1933), [KO Validated] Cytochrome *C* rabbit monoclonal antibody (A4912), β-actin rabbit monoclonal antibody (AC038), and Tubulin rabbit polyclonal antibody (AC008) were sourced from ABclonal Biotechnology Co., LTD (Wuhan, China).

### 2.2. Preparation of bimetallic iMWA nanosensitizers

The synthesis of mono or bimetallic nanotherapeutics followed a standardized procedure. Briefly, the specified quantity of TA (85 mg) was dissolved in Tris buffer (pH = 8.5) and combined with a solution containing $FeCl_3{\cdot}6H_2O$ and $CaCl_2$ (0.3 mg/mL and 0.15 mg/mL, 10 mL), respectively. The resulting mixture underwent stirring for 3 h at room temperature, followed by dialysis using a 3500 D molecular weight cutoff dialysis bag for one day to yield the bimetallic MWA nanosensitizer, named as CFT-NPs. For the preparation of single-metal nanotherapeutics, a predetermined amount of TA (85 mg) was dissolved in Tris buffer (pH = 8.5, 10 mL) and subsequently mixed with either $FeCl_3{\cdot}6H_2O$ (0.6 mg/mL, 10 mL) or $CaCl_2$ (0.3 mg/mL, 10 mL). Each resulting mixture underwent a subsequent dialysis process for one day to achieve the desired product characteristics, termed as FT-NPs or CT-NPs.

### 2.3. Characterization of bimetallic iMWA nanosensitizers

The morphologies were characterized by transmission electron microscopy (TEM; JEM-F200 FEI Tecnai G2 F20 FEI Talos F200s). The hydrodynamic diameter and Zeta potential were measured using a Zetasizer Nano ZS (Malvern Instruments Ltd., UK). UV–vis-NIR spectra were obtained with a UV–vis-NIR spectrophotometer (U3900, Hitachi Japan). Inductively coupled plasma mass spectrometry (ICP-OES) data were acquired using a 5100 SVDV system (Agilent, America). To detect the potential formation mechanism of biometallic nanosensitizers, the FT-IR spectra was obtained by using FT-IR spectroscopy (Spectrum Two, PerkinElmer, USA). The structures and interactions of the samples before and after adsorption were monitored using X-ray photoelectron spectroscopy (XPS) (Thermo escalab 250XI, USA).

The ionic release behavior was measured by dialysis method. In general, the CFT-NPs solution ($[Fe^{3+}]$ = 0.5 mM, 2 mL) was placed in a dialysis bag (MWCO = 3500 D) and the bag containing the sample was immersed in 10 mL of acetate buffer solution (ABS) at different pH (5.0, 7.4) in a shaking bath at 37 °C. At predetermined time intervals, 2 mL of the ABS solution was removed, and an equal volume of fresh ABS solution was added. The amount of $Fe^{3+}$ released from CFT was determined using the 1,10-phenanthroline method. Briefly, hydroxylamine hydrochloride (100 mg/mL, 100 μL) was added to the collected solution (500 μL) to reduce $Fe^{3+}$ to $Fe^{2+}$. Then, ABS buffer (pH = 5.0, 500 μL) was added to the above solution. Subsequently, 1,10-phenanthroline monohydrate (1 mg/mL, 100 μL) was added to the mixed solution, and the content of $Fe^{3+}$ released was calculated based on the UV–vis absorbance at 510 nm. The standard curve of $Fe^{3+}$ was established in the same way. The release rate of $Ca^{2+}$ from different nanotherapeutics was determined using a calcium colorimetric assay kit.

To assess the Fenton catalytic activity of CFT-NPs, we employed an established experimental method for methylene blue (MB) degradation [38]. This approach allowed us to monitor hydroxyl radical (·OH) production under various conditions. The detailed description of the evaluation process was as follows. First, CFT-NPs were dispersed in PBS buffer (pH = 5.0) to create a uniform suspension. Next, MB (100 μg/mL, 20 μL) and $H_2O_2$ (100 mM, 10 μL) were added to the suspension. The resulting mixture was then incubated for a period of time. At the end of the incubation period, the degradation of MB by ·OH was determined using UV–vis absorbance spectroscopy. CFT-NPs solution with PBS buffer at different pH (5.0, 7.4) was recorded by UV–vis absorbance spectrum at predetermined time intervals.

To assess the clearance of GSH of CFT-NPs. 100 μg of CT-NPs, FT-NPs and CFT-NPs were dispersed in 1 mL of 7.4 PBS, respectively, and then 1 mL 1 mg/mL of GSH solution was added, and allowed to stand for 30 min. After 10 min, the mixture was centrifuged at 10000 rpm for 5 min, and the supernatant was added to a centrifuge tube equipped with 4 mL of 7.4 PBS solution. Finally, 0.4 mL of DTNB was added, and allowed to stand for 5 min. The absorbance was then measured at 412 nm. The content of GSH can be obtained according to different absorbances and standard curves.

In order to study the sensitization of NPs, we established four groups, each with different concentrations of PBS, CT-NPs, FT-NPs, CFT-NPs (10, 50, 100, 150 μg/mL). Subsequently, 1 mL of the corresponding solutions was added to a 24-well plate. Immediately after, a microwave needle (Changcheng Medical) was inserted into the center of each well and operated for 1, 1.5 min at power levels of 1, 3, and 5 W. Infrared thermographic maps were captured using an infrared thermal imaging camera (Magnity Electronics Co., LTD), and the temperatures following MWA were recorded.

### 2.4. Cell culture and animals

Hepa 1–6 (murine) cell lines were procured from ATCC, while Hepa 1–6 luc (murine) cell lines were obtained from Meisen CTCC (Zhejiang Meisen Cell Technology Co., Ltd). Both Hepa 1–6 and Hepa 1–6 luc cells were cultured in DMEM medium (10 % FBS, 1 % penicillin-streptomycin). All cells were maintained at 37 °C and 5 % $CO_2$ in a humidified incubator. BALB/C nude mice were purchased and housed at the Guangxi Experimental Animal Center. Ethical approval for all animal experiments was obtained from the ethics committee of Guangxi Medical University Cancer Hospital (approval number: LW2024043).

In this study, treatments that mimicked incomplete tumor ablation were employed, which were collectively referred to as the iMWA group. Sublethal heat stress was applied to treat tumor cells in the cell investigation. Regarding the study involving animals, a tumor on a BALB/C nude mouse underwent partial MWA therapy under ultrasonography (MWA parameters: power = 3 W, duration = 1.5 min).

### 2.5. Sublethal heat treatment in vitro

To simulate iMWA therapy situation *in vitro*, an *in vitro* sublethal heat stress model was established. But owing to the inherent constraints of microwave ablation (MWA) devices, which particularly limit their usage range, we opted for an alternative approach to assess the therapeutic efficacy of induced microwave ablation (iMWA) on Hepa1-6 cells *in vitro* [39]. In brief, Hepa 1–6 cells were seeded in a 12-well plate and cultured for 24 h. Before heat treatment, the culture medium was removed, and the medium preheated to 43 °C was added. The plates were then immediately placed onto a 43 °C water bath apparatus for 15 min. After heat exposure, the culture plates were returned to the incubator for further detection.

### 2.6. Cellular internalization ability detection of bimetallic iMWA nanosensitizers

Hepa 1–6 cells were seeded in specialized confocal culture dishes at a density of $2.0 \times 10^5$ cells per dish and cultured for 24 h. Subsequently, the medium was replaced with 1.0 mL of serum-free medium (SFM) containing Cy5.5@CFT-NPs at a concentration of 100 μg/mL (Cy5.5: 10 μg/mL) and cultured for 0, 15, 30, 60, and 120 min, respectively. After washing with PBS twice, the cell nuclei were stained with Hoechst 33,342 for 15 min and washed with PBS twice before imaging observation by confocal laser scanning microscopy (CLSM) (Leica TCS SP8, Germany) at different time points. Blue fluorescence signal representing Hoechst 33,342 was recorded at $\lambda_{ex} = 346$ nm, $\lambda_{em} = 460$ nm, and the red fluorescence signal representing Cy5.5@CFT-NPs was recorded at $\lambda_{ex} = 680$ nm, $\lambda_{em} = 710$ nm.

To further assess the enrichment of $Ca^{2+}$ and $Fe^{2+}$ in Hepa 1–6 cells, $2.0 \times 10^5$ cells were seeded in confocal-specific culture dishes and cultured for 24 h. The medium was then replaced with 1.0 mL of SFM containing CFT-NPs at a concentration of 100 μg/mL and cultured for 2 h. Subsequently, the cell nuclei were stained with Hoechst 33,342 for 15 min and washed with PBS twice. The cells were then treated with the Ca-F07 probe (diluted at 1:1000) and Ferro-Orange probe (diluted at 1:500) and incubated for 20 min. After washing twice with PBS, the cells were observed by CLSM. Orange fluorescence, representing $Ca^{2+}$, was recorded at $\lambda_{ex} = 550$ nm and $\lambda_{em} = 581$ nm, and $Fe^{2+}$ was recorded at $\lambda_{ex} = 543$ nm and $\lambda_{em} = 580$ nm.

### 2.7. Detection of cell apoptosis

To assess the proapoptotic effect of drugs, $1.0 \times 10^5$ Hepa 1–6 cells were seeded per well in a 12-well low-attachment plate and cultured in SFM for 24 h to form tumor spheres. The group settings were as follows: $G_1$: Control; $G_2$: iMWA; $G_3$: iMWA + CT-NPs; $G_4$: iMWA + FT-NPs; $G_5$: CFT-NPs; $G_6$: iMWA + CFT-NPs (dose: 100 μg/mL). Subsequently, the cells were subjected to the different corresponding treatments in the $G_1$-$G_6$ groups ($G_{2,3,4,6}$ groups heat treatment conditions: the cells in plates were placed onto a 43 °C water bath apparatus for 15 min). After continuous culture for 12 h, Calcein AM/PI diluted at 1:1000 was added to the tumor spheres and incubated for 15 min before observation. The cytoplasmic green fluorescence representing living cells was recorded at $\lambda_{ex} = 494$ nm and $\lambda_{em} = 517$ nm, and the red fluorescence representing dead cells was recorded at $\lambda_{ex} = 535$ nm and $\lambda_{em} = 617$ nm.

The apoptosis rate of Hepa 1–6 cells was analyzed using the Annexin V-FITC apoptosis detection kit according to the manufacturer's protocol. For each well, $1.0 \times 10^5$ Hepa 1–6 cells were seeded in a 12-well plate and cultured for 24 h. Six groups were established ($G_1$: Control; $G_2$: iMWA; $G_3$: iMWA + CT-NPs; $G_4$: iMWA + FT-NPs; $G_5$: CFT-NPs; $G_6$: iMWA + CFT-NPs) for the different corresponding treatments ($G_{2,3,4,6}$ groups heat treatment conditions: the cells in plates were placed onto a 43 °C water bath apparatus for 15 min). After washing with PBS, cells were harvested and sequentially incubated with 5 μL FITC-labeled Annexin-V for 15 min and 5 μL of PI for 5 min. Subsequently, the cell apoptosis rates were analyzed using the FACS Canto II flow cytometer (B.D.).

For colony formation survival assays, $5.0 \times 10^2$ Hepa 1–6 cells were seeded per well in a 6-well plate and cultured for 24 h. Each group was treated accordingly ($G_{2,3,4,6}$ groups heat treatment conditions: the cells in plates were placed onto a 43 °C water bath apparatus for 15 min) and grouped as follows: $G_1$: Control; $G_2$: iMWA; $G_3$: iMWA + CT-NPs; $G_4$: iMWA + FT-NPs; $G_5$: CFT-NPs; $G_6$: iMWA + CFT-NPs. 14 days later, the cells were washed twice with PBS and immobilized with 4 % paraformaldehyde for 15 min, followed by staining with 1 % crystal violet. After drying, photographic recording was made using an inverted microscope.

To test the proapoptotic effect of materials on Hepa 1–6 cells and HUVECs per well $5.0 \times 10^3$ cells of Hepa 1–6 cells or HUVECs were seeded in a 96-well plate and cultured in 0.1 mL of DMEM for 24 h. The medium was then replaced with DMEM containing different concentration of CT-NPs, FT-NPs, CFT-NPs and cultured for 24 h respectively. Then, used the CCK-8 assay kit according to the manufacturer's protocol for examining the cell viability. Briefly, CCK-8 solution (10 μL) was added into each well, incubated in a 5 % $CO_2$ incubator for 3 h at 37 °C in the darkness, and then the absorbance at 450 nm was measured.

### 2.8. Detection of LPO levels

For each well, $1.0 \times 10^5$ Hepa 1–6 cells were seeded in a 12-well plate and cultured for 24 h. The six groups were designated as follows: $G_1$: Control; $G_2$: iMWA; $G_3$: iMWA + CT-NPs; $G_4$: iMWA + FT-NPs; $G_5$: CFT-NPs; $G_6$: iMWA + CFT-NPs. After various treatments in $G_1$-$G_6$ groups ($G_{2,3,4,6}$ groups heat treatment conditions: the cells in plates were placed onto a 43 °C water bath apparatus for 15 min), the cell nuclei were stained with Hoechst 33,342 for 15 min and washed with PBS twice. Subsequently, the cells were stained with DCFH-DA probes (1:1000 dilution), Thiol Tracker Violet dye solution (20 μM), and Image-iT™ Lipid Peroxidation dye solution (10 μM) for 10 min, then washed with PBS. The samples were observed and recorded using an inverted fluorescence microscope. Green fluorescence signal representing ROS was recorded at $\lambda_{ex} = 488$ nm and $\lambda_{em} = 525$ nm, and the relative intracellular GSH content was assessed by the blue fluorescence intensity at $\lambda_{ex} = 405$ nm and $\lambda_{em} = 525$ nm. Red fluorescence signal represented in C11-BODITY$^{581/591}$ was recorded at $\lambda_{ex} = 581$ nm and $\lambda_{em} = 591$ nm. Green fluorescence signal represents C11-BODITY$^{581/591}_{Oxidized}$ was recorded at $\lambda_{ex} = 488$ nm and $\lambda_{em} = 510$ nm.

And then, we conducted flow cytometry analysis to validate the ROS generation levels across different groups. For each well, $1.0 \times 10^5$ Hepa 1–6 cells were seeded in a 12-well plate and cultured for 24 h. Six groups were established ($G_1$: Control; $G_2$: iMWA; $G_3$: iMWA + CT-NPs; $G_4$: iMWA + FT-NPs; $G_5$: CFT-NPs; $G_6$: iMWA + CFT-NPs) for the different corresponding treatments ($G_{2,3,4,6}$ groups heat treatment conditions: the cells in plates were placed onto a 43 °C water bath apparatus for 15 min). After washing with PBS, cells were harvested and sequentially incubated with 1 μL FITC-labeled DCFH-DA probes for 15 min. Subsequently, the data was analyzed using the FACS Canto II flow cytometer (B.D.).

### 2.9. Detecting the effects on mitochondria

To assess changes in mitochondrial membrane potential, $1.0 \times 10^5$ Hepa 1–6 cells per well were seeded in a 12-well plate and cultured for 24 h. The cells were then treated according to the following groups: $G_1$: Control; $G_2$: iMWA; $G_3$: iMWA + CT-NPs; $G_4$: iMWA + FT-NPs; $G_5$: CFT-NPs; $G_6$: iMWA + CFT-NPs ($G_{2,3,4,6}$ groups heat treatment conditions: the cells in plates were placed onto a 43 °C water bath apparatus for 15 min), and further cultured for an additional 12 h. Subsequently, the JC-1 fluorescent probe (1:200) was added to the cells and incubated for 20 min. After washing with PBS twice, the cells were examined using a fluorescence microscope. At a high mitochondrial membrane potential,

JC-1 aggregated in the mitochondrial matrix to form a polymer (J-aggregate), producing red fluorescence recorded at $\lambda_{ex} = 585$ nm and $\lambda_{em} = 590$ nm. Conversely, at a low mitochondrial membrane potential, JC-1 could not aggregate in the mitochondrial matrix, existing as a monomer and emitting green fluorescence recorded at $\lambda_{ex} = 514$ nm and $\lambda_{em} = 529$ nm.

Moreover, we investigated changes in mitochondrial distribution, $2.0 \times 10^5$ Hepa 1–6 cells were seeded in confocal special culture dishes and cultured for 24 h. The cells were then treated according to the following groups: $G_1$: Control; $G_2$: iMWA; $G_3$: iMWA + CT-NPs; $G_4$: iMWA + FT-NPs; $G_5$: CFT-NPs; $G_6$: iMWA + CFT-NPs ($G_{2,3,4,6}$ groups heat treatment conditions: the cells in plates were placed onto a 43 °C water bath apparatus for 15 min), followed by an additional 12 h of culture. The cell nuclei were stained with Hoechst 33,342 for 15 min and washed with PBS twice. Subsequently, the M11 mitochondrial staining fluorescent probe (1:200) was added to the cells and incubated for 15 min. After washing with PBS twice, the cells were examined using CLSM. The red fluorescence signal representing mitochondria was recorded at $\lambda_{ex} = 579$ nm and $\lambda_{em} = 599$ nm.

### 2.10. Assessment of anti-tumor efficacy in vivo

To construct the liver cancer-bearing mice model, Hepa 1–6 luc cells ($3.0 \times 10^5$) were subcutaneously implanted on the right back of four-week-old athymic nude mice. When the tumor size was about 100 $mm^3$, the animal experiment was carried out, all tumor-bearing mice were randomly divided into six groups (n = 4): $G_1$: Control; $G_2$: iMWA; $G_3$: iMWA + CT-NPs; $G_4$: iMWA + FT-NPs; $G_5$: CFT-NPs; $G_6$: iMWA + CFT-NPs. Administered via the tail vein on 1, 3, and 5 days respectively (dose: 40 mg/kg/mice), and iMWA therapy under ultrasound was performed on 6 days (MWA parameters were set as follows: power = 3 W, duration = 1.5 min). Infrared thermographic maps were obtained using an infrared thermal imaging camera on mice after iMWA. From the 0 day, the xenograft tumor size was measured every 3 days with a vernier caliper, and the corresponding tumor volume was calculated according to the formula:

$$tumor\ volume = (length \times width \times width)/2$$

And performing luciferase imaging on mice during treatment, the fluorescence intensity was measured using the Lumina XR *in vivo* imaging system (Xenogen). Living Image (Ver.4.5, Xenogen) software was used to acquire an image sequence. The mice were sacrificed and the tumor was collected after 21 days, the tumor tissues were analyzed by H&E, IHC staining, terminal deoxynucleotidyl transferase-mediated dUTP nick-end labeling (TUNEL) staining, and western blot. As well, another 30 mice were divided into the same groups (n = 5) as mentioned above and received the corresponding treatments for survival analysis and observed for 60 days. When the tumor volume reached up to 2000 $mm^3$ or premature death of mice occurred, this time was designed as the endpoint.

To observe the distribution of NPs in the mice, Cy5.5@CFT-NPs were injected via the tail vein. Fluorescence images were captured at 0, 3, 6, 9, 12 and 24 h. The tumor-bearing mice were sacrificed and some main organs were collected to observe the biological distribution of NPs in the tumor, heart, liver, spleen, lung, and kidney after 24 h of treatment.

### 2.11. In vivo iMWA sensitization model

The sensitization effect and effective therapeutic properties of CFT-NPs combined with iMWA were verified in tumor-bearing mice. Next, the ability of CFT-NPs to enhance iMWA was explored in isolated pork liver. Two groups were divided, i.e., $G_1$: Control; $G_2$: iMWA + CFT-NPs (does: 8 mg/ml). After injecting CFT-NPs into pork liver, iMWA therapy under ultrasound was performed (MWA parameters were set as follows: power = 3 W, duration = 1.5 min). Subsequently, the treatment effects of the two groups were recorded and analyzed.

### 2.12. Western blotting test

After collecting tumor tissue, the total protein was extracted using RIPA lysis buffer supplemented with a protease and phosphatase inhibitor cocktail. Protein quantification was performed using the BCA protein assay kit. Equal amounts of protein from each group (10–20 μg) were separated on 12.5 % PAGE gels via electrophoresis (120 V, 80 min) and subsequently transferred to a PVDF membrane (250 mA, 90 min). The PVDF membranes were blocked with QuickBlock™ blocking buffer and were incubated with primary antibodies at 4 °C overnight. The primary antibodies used were as follows: GPX 4 (1:1000), calpain-1 (1:1000), ATP2B4 (1:1000), caspase 9 (1:1000), caspase 3 (1:1000), MMP 9 (1:1000), MMP 2 (1:1000), Cytochrome *C* (1:1000), Tubulin (1:5000) and β-actin (1:5000). After washing the membranes three times, they were incubated with HRP-labeled goat anti-rabbit IgG (H + L) for 1 h at room temperature. Following another wash with TBST again, BeyoECL Star detection reagent was added to the PVDF membrane, and the protein was visualized with the ChemiDoc Imaging System (Bio-Rad).

### 2.13. Immunofluorescence staining

Collect mouse tumors to prepare paraffin sections (deparaffinized and hydrated according to the aforementioned method). Ki-67 Polyclonal Antibody (PA5-19,462, Thermo Fisher USA) was used for Ki-67 staining at a dilution ratio of 1:1000. DCFH-DA (S0033-1, Beyotime, China) was employed for ROS staining at a dilution ratio of 1:1000. GPX 4 rabbit polyclonal antibody (A1933, Thermo, Beyotime, China) was used for GPX 4 staining at dilution ratio of 1:100. MMP9 Rabbit pAb (A0289, ABclonal, China) and MMP 2 Rabbit pAb (A6247, ABclonal, China) were used for MMP 9 and MMP 2 staining respectively, at a dilution ratio of 1:100. DAPI was applied to stain nuclei. Finally, the immunohistochemical staining images were captured and photographed using a biofluorescence microscope.

The pretreatment of tumor paraffin sections was identical to the previous method. After deparaffinization, 20 μg/mL Proteinase K was added dropwise to the sections to prepare the Proteinase K working solution. The sections were then incubated in a 37 °C incubator for 20 min. The sections were washed 3 times with PBS, followed by the addition of 50 μL of the prepared TUNEL detection solution, evenly applied dropwise. After incubation in the dark for 1 h, the PBS was taken out and the section were washed 3 times. After DAPI staining and mounting, the images were observed and photographed under a fluorescence microscope.

### 2.14. Biological safety evaluation

To evaluate the biosafety of CFT-NPs, an *in vivo* study was performed on 4-week healthy female nude mice (n = 4). The mice were injected intravenously with CFT-NPs at a dose of 40 mg/kg per mice and sacrificed on the 24th days. Blood samples were collected from the eyeballs on days 8, 16, and 24 for routine biochemical tests as well as assessments of liver and kidney function. The following indicators were evaluated: creatinine (CREA), urea, creatinine clearance (Ccr), alanine aminotransferase (ALT), aspartate aminotransferase (AST), uric acid (UA), white blood cell count (WBC), red blood cell count (RBC), and platelet count (PLT). Additionally, on the 24th day, the major organs including the heart, liver, spleen, lungs, and kidneys were collected and histologically examined using hematoxylin and eosin (H&E) staining.

### 2.15. Statistical analysis

Statistical analysis was conducted using GraphPad Prism software (version 8.01), and inter-group statistical comparisons were performed using a one-way ANOVA or Student *t*-test. All statistical tests were conducted with two-tailed significance. The results obtained from these

tests are presented as mean ± SD (standard deviation) to indicate the variability within each group. Statistical significance was denoted as follows: *$P < 0.05$, **$P < 0.01$, ***$P < 0.001$, and ****$P < 0.0001$, indicating increasing levels of significance.

## 3. Results and discussion

### 3.1. Bimetallic iMWA nanosensitizer design and its physicochemical characterization

Inspired by the robust coordination abilities exhibited by phenolic hydroxyl groups within TA structures with metal ions [40–42], we have adopted a methodology based on previous reports to construct a bimetallic nanosensitizer utilizing TA, iron ($Fe^{3+}$) and calcium ($Ca^{2+}$) ions, as illustrated in Fig. 1**A**. TEM images verified the formation of nanoscale particles including CFT-NPs, CT-NPs, and FT-NPs, and element mapping images demonstrated the presence of Fe and Ca components inside CFT-NPs (Fig. 1**B, Figures S1-S2**). Dynamic light scattering (DLS) analysis further affirmed the formation of nanoscale particle size with a negative zeta potential of about −15 to −30 mV and their stability in both water, culture medium and 10 % FBS (Fig. 1**C, D and Figures S5-S7**), prove that the CFT-NPs, CT-NPs, and FT-NPs exhibit good stability in different solutions. In addition, hemolysis analysis showed good blood compatibility of CFT-NPs (**Figure S8**), indicating their potential for targeted delivery to tumor sites with biosafety and prolonged blood circulation.

To explore the potential interactions between these components, we conducted a series of experiments. FT-IR spectra (**Figure S3**) provided further evidence of the coordination reaction between $Fe^{3+}$/$Ca^{2+}$ and TA. Upon comparing the FT-IR spectra of TA with CT-NPs, FT-NPs, and CFT-NPs, notable peak shifts can be observed. Specifically, the hydroxyl absorption peaks of CT-NPs, FT-NPs, and CFT-NPs exhibit red shifts compared to TA, originally positioned at 3392 $cm^{-1}$, and are observed at approximately 3410, 3398, and 3400 $cm^{-1}$, respectively. This red shift was attributed to the complexation of hydroxyl groups in TA with $Ca^{2+}$ and $Fe^{3+}$ ions, coupled with the formation of hydrogen bonds between hydroxyl groups. Furthermore, the characteristic peaks associated with aromatic C = C and C–O stretching in TA were situated at 1535, 1447, 1318, and 1194 $cm^{-1}$. In contrast, these peaks underwent slight displacements in CFT-NPs, shifting to 1533, 1446, 1323, and 1202 $cm^{-1}$, accompanied by variations in peak intensities. This variation suggests that the interaction between hydroxyl groups and $Fe^{3+}$ and $Ca^{2+}$ ions had a discernible influence on the aromatic groups. Concurrently, the

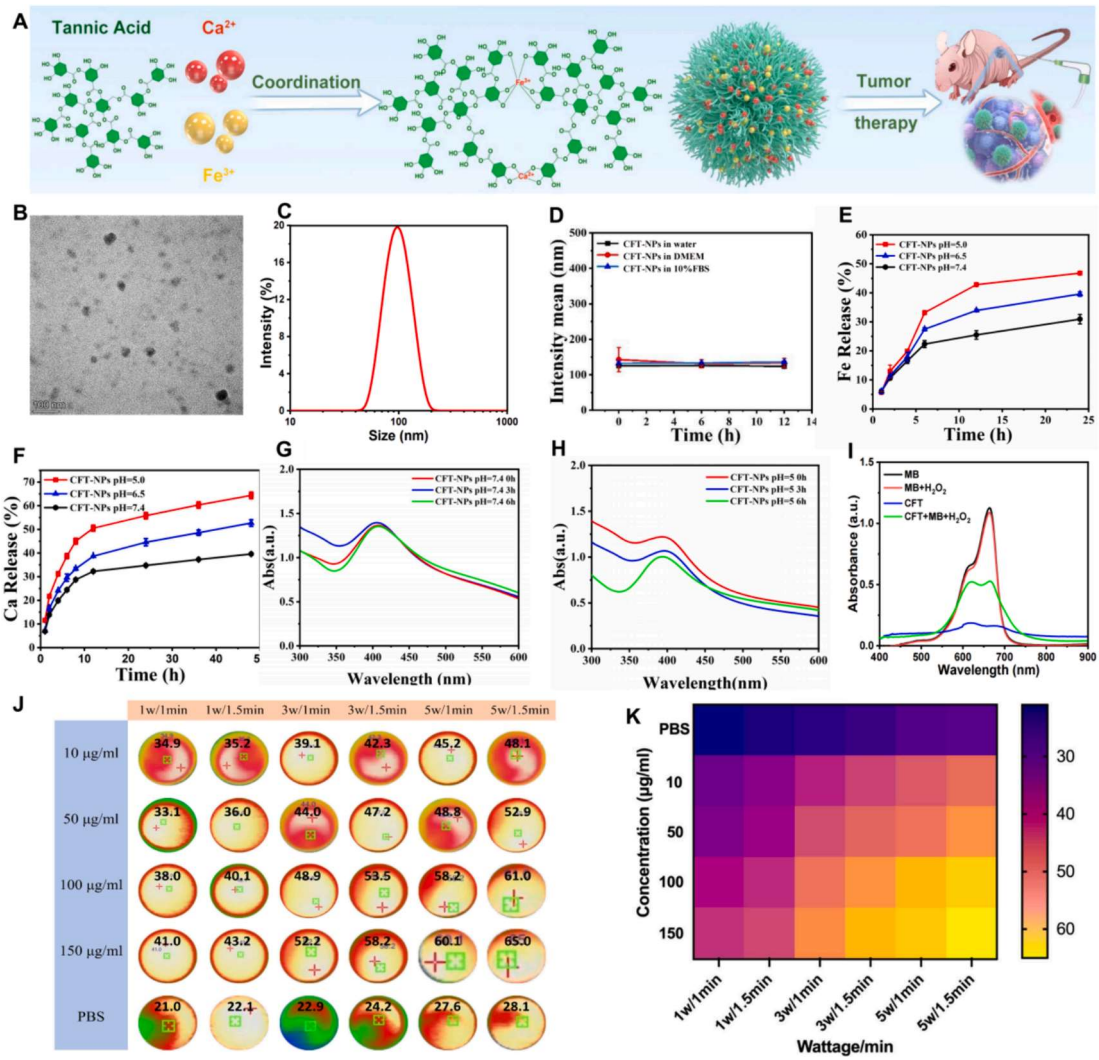


**Fig. 1. Characterization of physicochemical properties of the iMWA nanosensitizer.** (A) schematic illustration of the construction process of CFT-NPs; (B) TEM image of CFT-NPs, the scar bar is 100 nm; (C) size determination of CFT-NPs by DLS; (D) size variation of CFT-NPs when incubated in water, DMEM cell culture medium or 10 %FBS; (E) $Fe^{3+}$ and (F) $Ca^{2+}$ release profiles under acidic (pH = 5.0, pH = 6.5) or neutral (pH = 7.4) conditions of CFT-NPs; UV–vis absorption spectra of CFT-NPs under (G) neutral and (H) acidic conditions; (I) UV–vis absorption spectra of CFT-NPs and MB after being incubated with or without $H_2O_2$; (J) Infrared thermographic images and (K) corresponding volcanic map of CFT-NPs solutions at different concentration under MWA at different power.

peak at 1086 $cm^{-1}$ corresponds to the C–O–C stretching mode of TA. However, in the spectra of CT-NPs, FT-NPs, and CFT-NPs, the carbonyl-related peaks appeared at approximately 1714, 1714, and 1713 $cm^{-1}$, exhibiting a blue shift relative to TA's peak at 1716 $cm^{-1}$. These spectral changes served as confirmatory evidence of the successful preparation of CT-NPs, FT-NPs, and CFT-NPs. Moreover, XPS analysis had definitively validated the presence of Ca and Fe components in CFT-NPs (**Figure S4**). Specifically, the binding peaks at 724.6 and 713.6 eV correspond to the 2p3/2 and 2p1/2 states of $Fe^{2+}$, whereas the peaks at 717.6 and 710.2 eV represent the 2p3/2 and 2p1/2 states of $Fe^{3+}$. This revelation suggested that CFT-NPs predominantly established a coordination network through unsaturated double-ligand complexation. Consequently, the significant content of reduced iron and unsaturated coordination bonds in CFT-NPs favors the intracellular pH-induced iron release and facilitates the execution of the Fenton reaction.

Additionally, considering that coordinate interactions in CFT-NPs are sensitive to the intracellular acid environment, the release behavior of $Ca^{2+}$ and $Fe^{3+}$ ions at different pH values was investigated to validate their pH-sensitive characteristics. As expected, under normal physiological conditions (pH 7.4), the amount of $Fe^{3+}$ and $Ca^{2+}$ released from the CFT-NPs nanosensitizer was approximately 30 % after 24 h of incubation. However, at a reduced pH matching the acidity of tumor tissues (pH 6.5), the released amounts of $Fe^{3+}$ and $Ca^{2+}$ increased to about 40 % and50% respectively. Certainly, it is noteworthy that the rate of release of $Fe^{3+}$ and $Ca^{2+}$ escalates in response to a decrease in pH levels (Fig. 1**E, F**). A similar trend could also be observed in CT-NPs and FT-NPs (**Figure S9**). This rapid release could result in the accumulation of $Fe^{3+}$ and $Ca^{2+}$ within cells, promoting apoptosis of tumor cells. UV spectroscopy results showed an obvious absorption decrease of CFT-NPs when incubated in an acidic solution compared to that in a neutral solution, suggestive of the structure disruption under acidic conditions (Fig. 1**G, H**). Given the ability of $Fe^{2+}$ to catalyze $H_2O_2$ to generate ·OH through the Fenton reaction, we selected MB, a dye degradable by·OH, as an indicator. Fig. 1**I** illustrated a significant decrease in absorbance when MB was incubated with $H_2O_2$ and CFT-NPs, suggesting the Fenton reaction activity of CFT-NPs. GSH, as antioxidant substance in tumor cells, has the ability to mitigate ROS levels and cytotoxicity, thereby diminishing the efficacy of ROS-based therapeutic strategies. To determine the GSH content, we evaluated the GSH clearance capabilities of CT-NPs, FT-NPs, and CFT-NPs. Notably, a significant consumption of GSH was observed in the CFT-NPs group. As illustrated in **Figure S10**, the absorption curve of CFT-NPs at 412 nm exhibits the weakest intensity, indicating the lowest GSH content. Conversely, the changes observed in CT-NPs and FT-NPs at 412 nm were insignificant, thus confirming that CFT-NPs efficiently convert GSH to GSSG, thereby depleting GSH levels and enhancing the effectiveness of ROS-based treatments. Subsequently, we assessed the ability of nanosensitizer to enhance heating under low-frequency microwave stimulation. The results demonstrated the positive correlation between the heating effect and the concentration of CFT-NPs, microwave power, and time (Fig. 1**J, K**). Moreover, CFT-NPs demonstrated the best conversion efficiency of electromagnetic energy into heat compared to that of CT-NPs and FT-NPs, which was due to the synergistic effect of $Fe^{3+}$ and $Ca^{2+}$ (**Figure S11 and 12**). Meanwhile, the good stability of the heating capacity of CFT-NPs was further verified by studying their temperature-increasing behaviors during five on/off cycles (**Figure S13**). Collectively, coordination-driven CFT-NPs have been successfully constructed, which demonstrated good stability, pH-responsive $Ca^{2+}$/$Fe^{3+}$ release behaviors, Fenton reaction activity, and enhanced conversion efficiency of electromagnetic energy into heat, showcasing their great potential in tumor-specific therapy.

### 3.2. Cellular uptake and cytotoxicity of bimetallic iMWA nanosensitizer

Given the prominent thermal properties of CFT-NPs under iMWA, the cellular uptake behavior of CFT-NPs was initially detected in Hepa1-6 cells using a confocal microscope, as effective intracellular uptake is a precondition for achieving a satisfactory antitumor effect. As shown in Fig. 2**A and Figure S14**, a gradual increase in intracellular fluorescence intensity was observed over time, with CFT-NPs eventually achieving full distribution throughout the entire cell body after 120 min of treatment, indicating their great potential to exert a killing effect on tumor cells. As demonstrated by other study, intracellular $Fe^{3+}$ released from CFT-NPs can be reduced to $Fe^{2+}$ by TA. When these ions encounter reducing agents present within tumor cells, such as glutathione (GSH) or tannic acid liberated from the nanosensitizer, they undergo reduction to form divalent iron ions ($Fe^{2+}$). Subsequently, the $Fe^{2+}$ ions efficiently catalyze intracellular hydrogen peroxide, resulting in the generation of reactive oxygen species (ROS) and thus enabling the implementation of chemodynamic therapy. Therefore, we evaluated the accumulation of $Fe^{2+}$ and $Ca^{2+}$ ions in cells, respectively. Notably, the Ferro-Orange probe was employed for $Fe^{2+}$ detection and higher fluorescence density in cells treated with iMWA + CFT-NPs compared to the control group (Fig. 2**B, C**). Obviously, the increase $Fe^{2+}$ density originated from the reduction of $Fe^{3+}$ in CFT-NPs, further confirming that $Fe^{3+}$ can be reduced to $Fe^{2+}$. Moreover, both $Fe^{2+}$ and $Ca^{2+}$ ions levels increased approximately threefold compared to the control group, as depicted in Fig. 2**B-D**. This increase was attributed to the dissociation of $Fe^{3+}$ and $Ca^{2+}$ ions from CFT-NPs, indicating that the rupture of CFT-NPs was pH-driven and was in accordance with the ions' release behavior.

Encouraged by the satisfactory cellular uptake ability, we examined the tumor cell-killing effects of CFT-NPs. Firstly, Crystal violet staining was performed, and the results showed that compared with the control group, iMWA alone could hardly inhibit cell cloning activity, while CFT-NPs led to a 40 % reduction in cell colony formation (Fig. 2**E, G**), proving the cytotoxicity caused by CFT-NPs after cellular uptake. Meanwhile, the lowest number of cell colonies number was observed in the iMWA + CFT-NPs group, indicating that the $Fe^{2+}$ reduced from $Fe^{3+}$ combined with $Ca^{2+}$ in enhancing the iMWA effect. Moreover, the cytotoxic effects of Hepa1-6 cells exposed to nanosensitizers were assessed *in vitro* using the CCK-8 assay. As illustrated in **Figure S15**, both FT-NPs and CT-NPs exhibited toxicity towards Hepa1-6 cells, whereas CFT-NPs displayed a significantly heightened cytotoxic potential, which was dependent on the concentration of nanosensitizers. This enhanced ability of CFT-NPs to inhibit Hepa1-6 cells proliferation is primarily attributed to the synergistic effect of dual metal ions. As anticipated, there was negligible cytotoxicity on normal cells for CT-NPs, FT-NPs, and CFT-NPs, even at a concentration of 200 μg/mL (**Figure S15**). Subsequently, Annexin $V^+$/PI staining was conducted to further evaluate the *in vitro* antitumor efficiency of CFT-NPs. As shown in Fig. 2**F and H**, iMWA did not induce obvious cell apoptosis, but CFT-NPs alone could result in 10 % cell apoptosis compared to the control group, suggestive of the ferroptosis and $Ca^{2+}$ overload-induced apoptosis. Moreover, there were 25 % and 36 % Annexin $V^+$ positive cells in iMWA + CT-NPs and iMWA + FT-NPs groups, respectively, while approximately 58 % of Annexin $V^+$ positive cells could be detected in the iMWA + CFT-NPs group, indicative of the synergistical enhancement of the antitumor effect of iMWA through the promotion of cell apoptosis by the bimetallic ions within CFT-NPs.

To further investigate the tumor penetration and killing effect, we created tumoroids to mimic *in vivo* tumor conditions. Notably, iMWA alone failed to induce any cell death within the tumor spheroids due to the limited heat production of low-frequency microwaves (Fig. 2**I**, **Figure S16**). In addition, CFT-NPs alone primarily killed cells at the periphery of the tumoroids, while the inner cells remained viable. This is likely due to the limited antitumor effect achieved through the bimetallic ions, which is consistent with the aforementioned results on cell apoptosis. Surprisingly, when iMWA was combined with NPs, a higher number of inner cells died. In particular, iMWA + CFT-NPs caused the highest number of cell deaths compared to iMWA + CT-NPs and iMWA + FT-NPs. This observation suggests that nanosensitizer enhance the iMWA effect, with CFT-NPs exhibiting the most performance, induce a

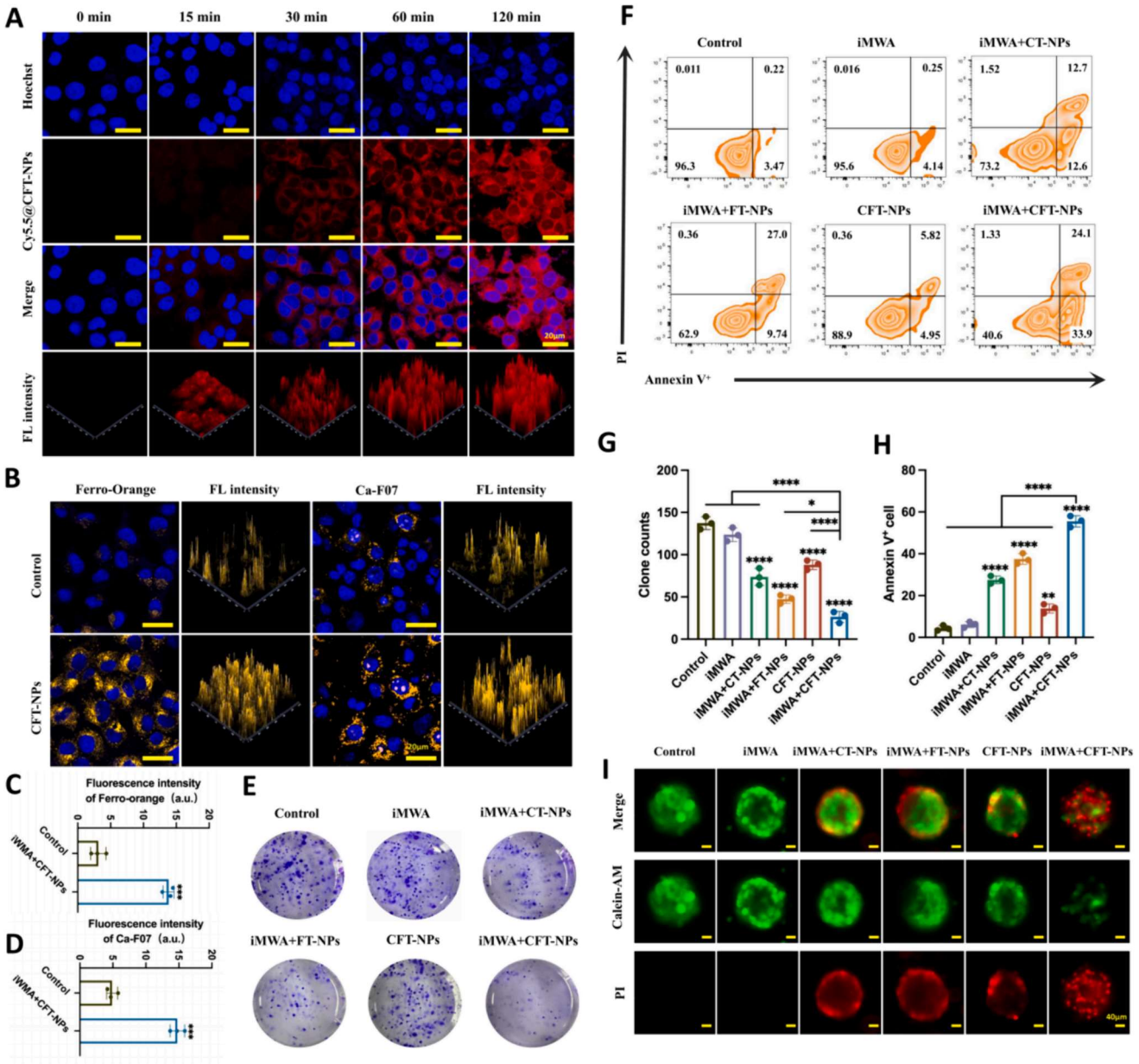


**Fig. 2.** ***In vitro*** **evaluation of cell behavior with iMWA nanosensitizer treatments.** (A) CLSM images of Hepa 1–6 cells after incubation with Cy5.5@CFT-NPs for different durations to observe the cellular uptake of Cy5.5@CFT-NPs; (B) CLSM images of Hepa 1–6 cells stained with $Fe^{2+}$ indicator (i.e., Ferro-Orange) and $Ca^{2+}$ indicator (i.e., Ca-F07) to observe the cellular uptake; Corresponding quantitative (C) Ferro-Orange and (D) Ca-F07 fluorescence signal intensity in Hepa 1–6 cells; (E) Cloning of Hepa 1–6 cells and (G) corresponding calculation of colonies counts after different treatments; (F) FCM patterns of Hepa 1–6 cells after Annexin V-FITC/PI co-staining and (H) corresponding quantification after different treatments; (I) CLSM calcein AM/PI co-staining images of Hepa 1–6 cells spheroids after different treatments to directly evaluate live and dead cells. Data are expressed as mean ± SD (n = 3). The significance analysis for inter-group statistical comparisons was conducted using ANOVA, and *$P < 0.05$, **$P < 0.01$, ***$P < 0.001$, and ****$P < 0.0001$.

large number of tumor cells apoptosis. Overall, the combination of iMWA and CFT-NPs holds great promise for effectively inducing tumor cell death.

### 3.3. *Mechanism of bimetallic iMWA nanosensitizer-induced mitochondria damage*

As previously documented, iron ions are crucial transition metals in biological systems, essential for processes such as oxygen metabolism and electron transport. Additionally, calcium ions ($Ca^{2+}$) play a fundamental role in the physiological and biochemical functions of cells, participating in signal transduction pathways [43,44]. Therefore, we aimed to investigate the mechanisms underlying the CFT-NPs-induced cytotoxicity in Hepa1-6 cells. We chose DCFH-DA as a fluorescent probe sensitive to ROS to assess intracellular ROS levels using CLSM. As shown in Fig. 3**A and G**, iMWA alone did not significantly increase ROS expression. However, the addition of CT-NPs or FT-NPs during iMWA treatment led to an increase in ROS levels, suggesting that the ions within CFT-NPs could disrupt redox balance in cells. Notably, CFT-NPs alone were sufficient to induce an increase in ROS levels, likely due to the elevated levels of $Fe^{2+}$ and $Ca^{2+}$ ions. Furthermore, the combination of iMWA and CFT-NPs resulted in the highest ROS level compared to that in the other groups, indicating that iMWA significantly potentiated the effect of CFT-NPs on tumor redox state. Furthermore, the quantitative analysis of ROS production via flow cytometry corroborated the findings obtained from CLSM, as depicted in **Figure S17**. Subsequently,

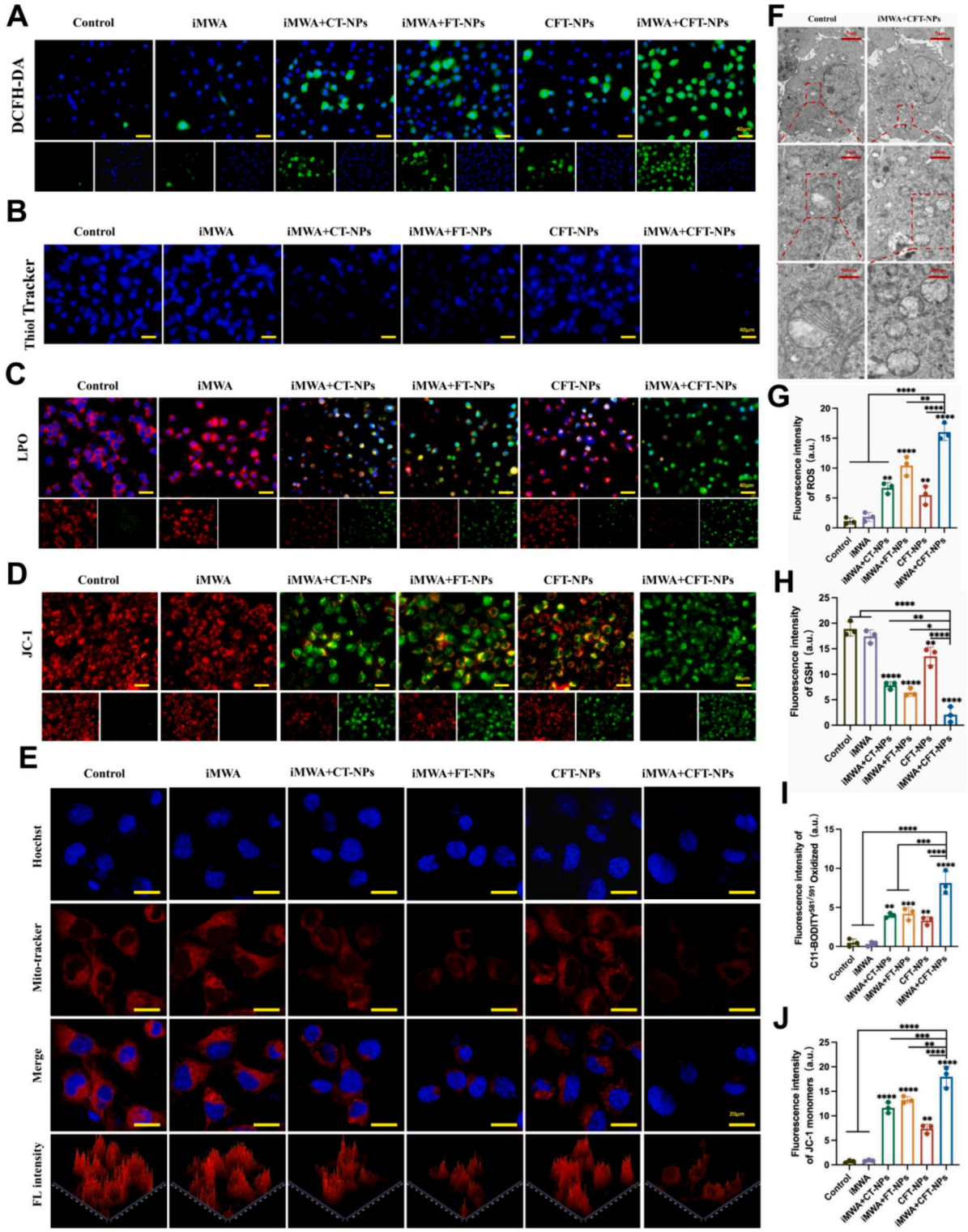


**Fig. 3.** ***In vitro*** **mitochondria damage evaluations with MWA nanosensitizer.** (A) CLSM images and (G) corresponding quantitative ROS fluorescence signal intensity of Hepa 1–6 cells after ROS indicator (i.e., DCFH-DA) staining post-different treatment; (B) CLSM images and (H) corresponding quantitative GSH depletion values of Hepa 1–6 cells after GSH indicator (i.e., ThiolTracker) staining post-different treatments; (C) CLSM images of Hepa 1–6 cells after LPO indicator (i.e., C11-BODIPY$^{581/591}$) staining post-different treatments, and (I) corresponding quantification of C11-BODIPY$^{581/591}$ oxidized form reflecting LPO level; (D) CLSM images of Hepa 1–6 cells after JC-1 probe staining post-different treatments, and (J) corresponding quantification of JC-1 monomers, which positively correlate with the degree of mitochondria damages; (E) CLSM images of Hepa 1–6 cells after mitotracker staining post-different treatments for directly evaluating mitochondria damages; (F) Bio-TEM images of Hepa 1–6 cells treated with iMWA + CFT-NPs and control, and scale bars: 5 μm, 1 μm, and 500 nm, wherein mitochondrias are circled by rectangle with red dotted lineablation and enlargered marked. Data are expressed as mean ± SD (n = 3). The significance analysis for inter-group statistical comparisons was conducted using ANOVA, and *$P < 0.05$, **$P < 0.01$, ***$P < 0.001$, and ****$P < 0.0001$.

to further explore the impact of redox state disruption on cells, we evaluated the expression of the reductive biomarker GSH and the level of LPO in cells. Notably, iMWA treatment alone had minimal effects on GSH expression (Fig. 3**B and H)**, while the addition of NPs significantly downregulated GSH production. In particular, the combination of iMWA and CFT-NPs treatment led to the lowest GSH levels. Meanwhile, LPO detection was performed using a lipid-soluble ratiometric fluorescent indicator C11-BODIPY$^{581/591}$. This probe undergoes a shift in excitation maximum from 581 to 500 nm and emission maximum from 591 to 510 nm upon oxidation. As shown in Fig. 3**C, I, and** Figure S18, increased green signals and reduced red signals were observed in iMWA + CFT-NPs treated cells, indicating increased lipid oxidation. It is well established that LPO disrupts membrane organization, leading to functional loss and modifications of proteins and DNA bases, and has been implicated in various disease pathologies. These data suggest that the CFT-NPs amplify ROS production in cells under iMWA treatment, disrupting biological processes and electron transport, ultimately leading to lipid oxidation and GSH downregulation.

Previous reports have suggested that the production of ROS disrupts the mitochondrial energy metabolism in cancer cells [45]. In light of this, we aimed to investigate mitochondrial activity and structural changes following various treatments. To assess mitochondrial membrane potential (ΔΨm), we utilized JC-1 staining. As indicated in Fig. 3**D, J**, and **Figure S19**, the presence of distinct JC-1 aggregate red signals was observed in both the control and iMWA groups, indicating that iMWA alone treatment preserved functional mitochondria with a high ΔΨm. However, when treated with CFT-NPs and iMWA, there was a reduction in JC-1 aggregate formation and an increase in the presence of JC-1 monomers within the cells. This observation could be attributed to the $Fe^{2+}$ and $Ca^{2+}$ overload-induced overproduction of intracellular ROS, as previously mentioned. Furthermore, mitochondrial mass and activities were evaluated using Mito-tracker staining, which revealed a decrease in mitochondrial mass and altered structure following NPs' treatment (Fig. 3**E and** Figure S20). The results obtained using both JC-1 and Mito-tracker probes were highly consistent, highlighting the changes in ΔΨm and mitochondrial damage experienced by Hepa1-6

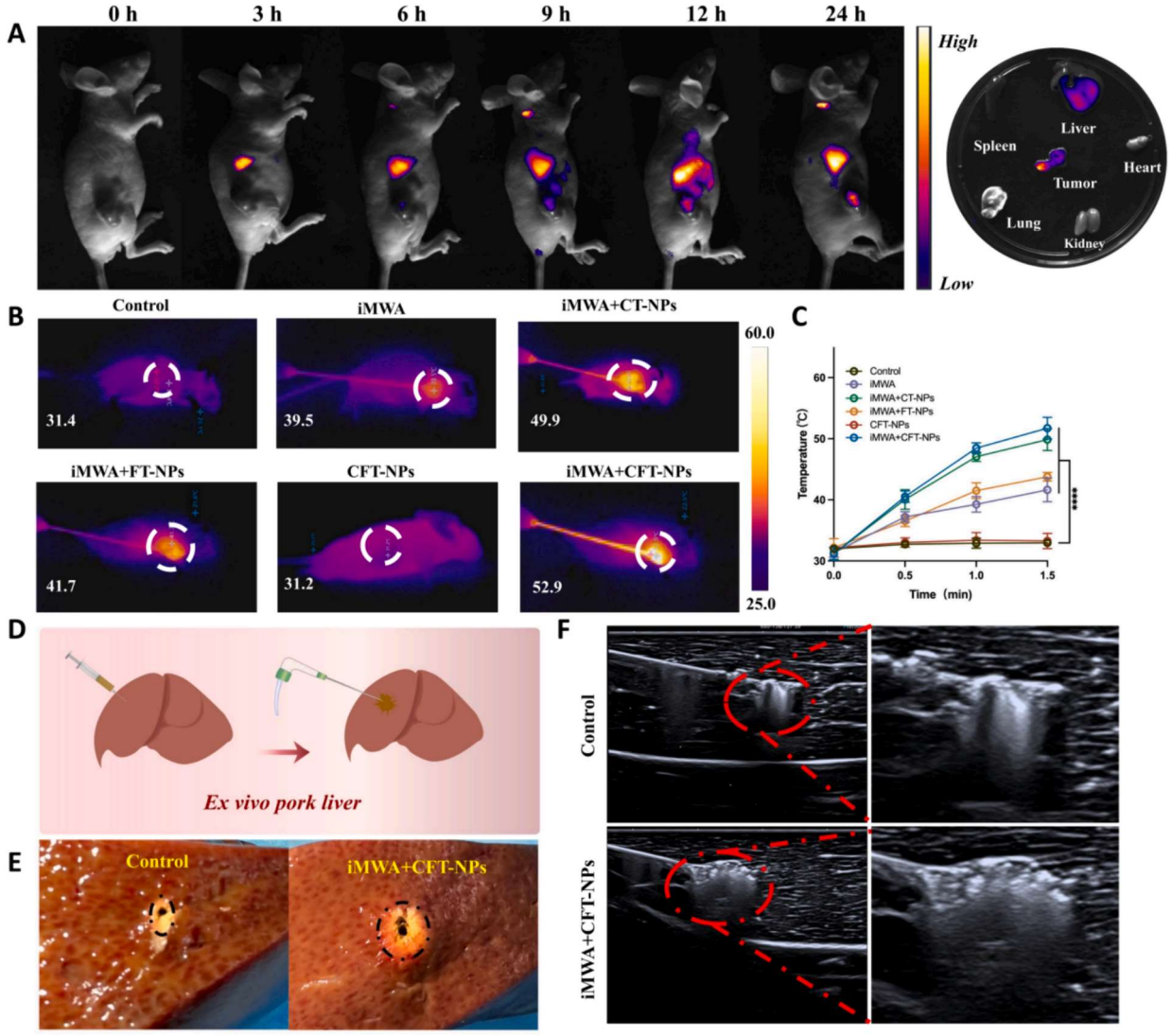


**Fig. 4.** (A) Time-dependent fluorescence images of Hepa 1–6 tumor-bearing mice injected with Cy5.5@CFT-NPs to observe the biological distribution of CFT-NPs in tumor and major organs (n = 3); (B) infrared thermographic images of each group of Hepa 1–6 tumor-bearing mice after different treatments and (C) the temperature line graph at different time points; (D) Schematic of the ex vivo iMWA ablation on pork liver; (E) digital photos of ablated pork liver tissues after different treatments, that are iMWA alone and iMWA + CFT-NPs, wherein ablated zones are circled by ellipses with black dotted line ablation; (F) ultrasound images of pork liver after iMWA ablation (MWA parameters were set as follows: power = 3 W, duration = 1.5 min), wherein ablated zones are circled by ellipses with red dotted line ablation and enlarge. Data are expressed as mean ± SD (n = 3). The significance analysis for inter-group statistical comparisons were conducted using ANOVA, and *$P < 0.05$, **$P < 0.01$, ***$P < 0.001$, and ****$P < 0.0001$.

cells following iMWA + NPs treatment. To gain further insights into mitochondrial structure, we employed BIOSEM analysis. The results confirmed notable structural alterations in mitochondria, including swelling and the loss of mitochondrial cristae (Fig. 3**F**). These changes are crucial for Cytochrome *C* (Cyt c) release during the intrinsic pathway of apoptosis. Collectively, these findings demonstrated that the released $Fe^{2+}$ and $Ca^{2+}$ from CFT-NPs promote ROS production, cause mitochondrial damage, and ultimately enhance the therapeutic effect of CFT-NPs in combination with iMWA treatment.

### 3.4. Biodistribution and microwave sensitization efficiency of iMWA sensitizers

Prior to studying the microwave sensitization effects of NPs *in vivo*, we first examined their biodistribution after intravenous injection using Hepa1-6 tumor-bearing mice as an animal model. As shown in Fig. 4**A**, we observed efficient accumulation of NPs at the tumor site over time, likely due to the EPR effect. Notably, there was almost no retention of NPs retention in the spleen, heart, lung, and kidney, while obvious signals were detected in the liver, suggesting that it is the main

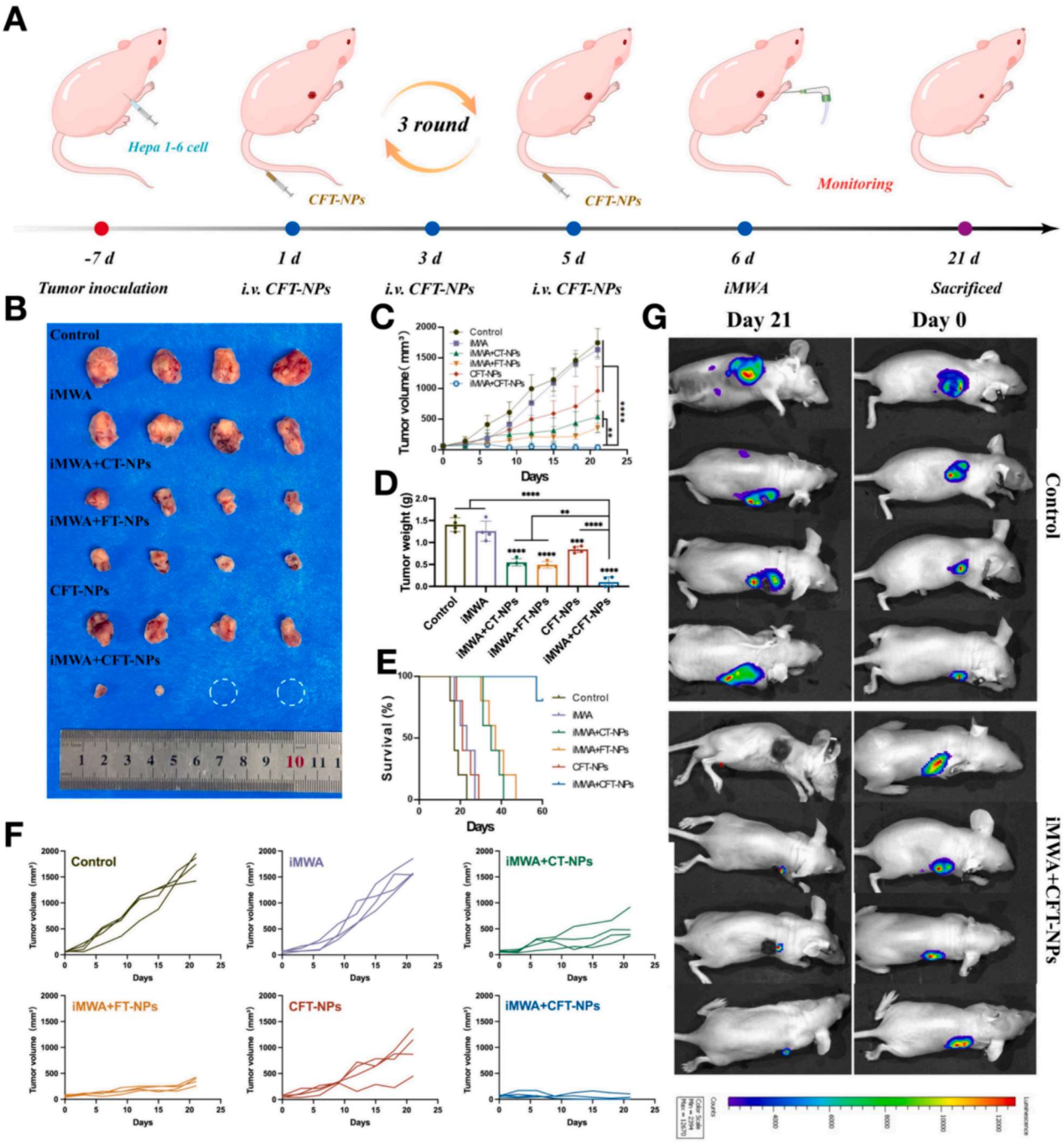


**Fig. 5. Antitumor treatment of MWA nanosensitizer *in vivo*.** (A) In vivo schematic procedures using iMWA + CFT-NPs to repress tumor; (B) digital photos and (D) weights of isolated tumors from Hepa 1–6 tumor-bearing mice in different groups at the end of experimental period; (C and F) time-dependent tumor volume profiles of tumors in different treatment groups (n = 4); (E) survival periods of tumor-bearing mice in different groups; (G) Hepa 1–6-Luc tumor-bearing mice were subjected to whole-body bioluminescence imaging at the end of experimental period. Data are expressed as mean ± SD (n = 4). The significance analysis for inter-group statistical comparisons was conducted using ANOVA, *and *P < 0.05, **P < 0.01, ***P < 0.001, and ****P < 0.0001.*

metabolism organ for NPs. Motivated by the positive outcomes, we further investigated the potency of NPs to potentiate the microwave heating efficacy *in vivo*. As recorded using a thermal infrared camera (Fig. 4**B, C and** Figure S21), compared to the control group, tumors treated solely with intratumoral iMWA exhibited a temperature increase to around 39.5 °C. Despite the direct application of the free ion group, the heating effect observed was inadequate, showing no significant deviation from iMWA-alone group. After free ions incorporated into NPs, CFT-NPs alone did not induce a temperature increase when compared to the control group (~31.4 °C). Upon exposure to iMWA, the temperature in tumors treated with CT-NPs and CFT-NPs showed a much faster escalation and stabilized around 50 °C. In contrast, FT-NPs showed only a subtle increase in temperature (~41.7 °C), possibly due to the superior sensitization ability of $Ca^{2+}$. This disparity is primarily attributed to the fact that our nanosensitizer encapsulating $Fe^{3+}$ and $Ca^{2+}$ ions are able to effectively deliver these ions to tumor tissue via the EPR effect, ultimately achieving a bimetallic sensitization effect. Notably, the combination of iMWA and CFT-NPs led to a rapid temperature increase confined to the tumor site, without affecting the surrounding tissue. Furthermore, we observed that a significant amount of NPs could be injected and retained within the porcine liver, serving as a mimic for large tumors. This enabled more rapid microwave heating and a larger thermal ablation volume (Fig. 4**D-F**). Collectively, these results demonstrate that CFT-NPs are promising and effective microwave-sensitive biomaterials that can concentrate the microwave heating zone to the tumor site.

### 3.5. *In vivo* therapeutic efficiency evaluation

Based on the preceding studies, we evaluated the therapeutic efficacy of NPs-assisted iMWA in mice harboring subcutaneous Hepa1-6 tumors. The specific therapeutic regimes were outlined in Fig. 5**A**. Once the tumor volumes reached approximately 100 $mm^3$, six groups of mice received the following treatments: $G_1$, a control group with saline injection; $G_2$, iMWA alone; $G_3$, CT-NPs injection followed by iMWA (iMWA + CT-NPs); $G_4$, FT-NPs injection followed by iMWA (iMWA + FT-NPs); $G_5$, CFT-NPs injection alone; and $G_6$, CTF-NPs followed by iMWA (iMWA + CFT-NPs). As depicted in **Figure S22**, ultrasound images displayed the tumor's condition under MWA, successfully enlarging the area of MWA within tumors. Furthermore, iMWA alone had minimal impact on tumor growth, confirming its limited ability to restrict tumor growth using low-frequency microwaves (Fig. 5**B-D**). Interestingly, even without microwave exposure, CFT-NPs treatment obviously inhibited tumor growth compared to the control group, presumably due to the metal ions' effect on tumor cells. Remarkably, the combination of iMWA + CFT-NPs achieved complete tumor ablation without noticeable tumor recurrence for up to 21 days (Fig. 5**G and** Figure S23), attributed to the microwave sensitization, ferroptosis, and intracellular $Ca^{2+}$ homeostasis disruption. The tumor volume results aligned with excised tumor photography and weight measurements (Fig. 5**C, D, and F**). Notably, there was no significant changes in body weight among mice after different treatments, indicative of no systematic toxicity from the combination of NPs and microwave therapy (**Figure S24**).

Additionally, mice treated with iMWA + CFT-NPs demonstrated a median survival time exceeding 60 days (Fig. 5**E**), significantly surpassing the 36 days and 38 days observed in the iMWA + CT-NPs and iMWA + FT-NPs groups respectively. This further corroborated our *in vitro* cellular experimental findings, highlighting the synergistic effect of $Fe^{2+}$ and $Ca^{2+}$ in enhancing the therapeutic potency of hyperthermia. The superior therapeutic outcomes achieved with iMWA + CFT-NPs

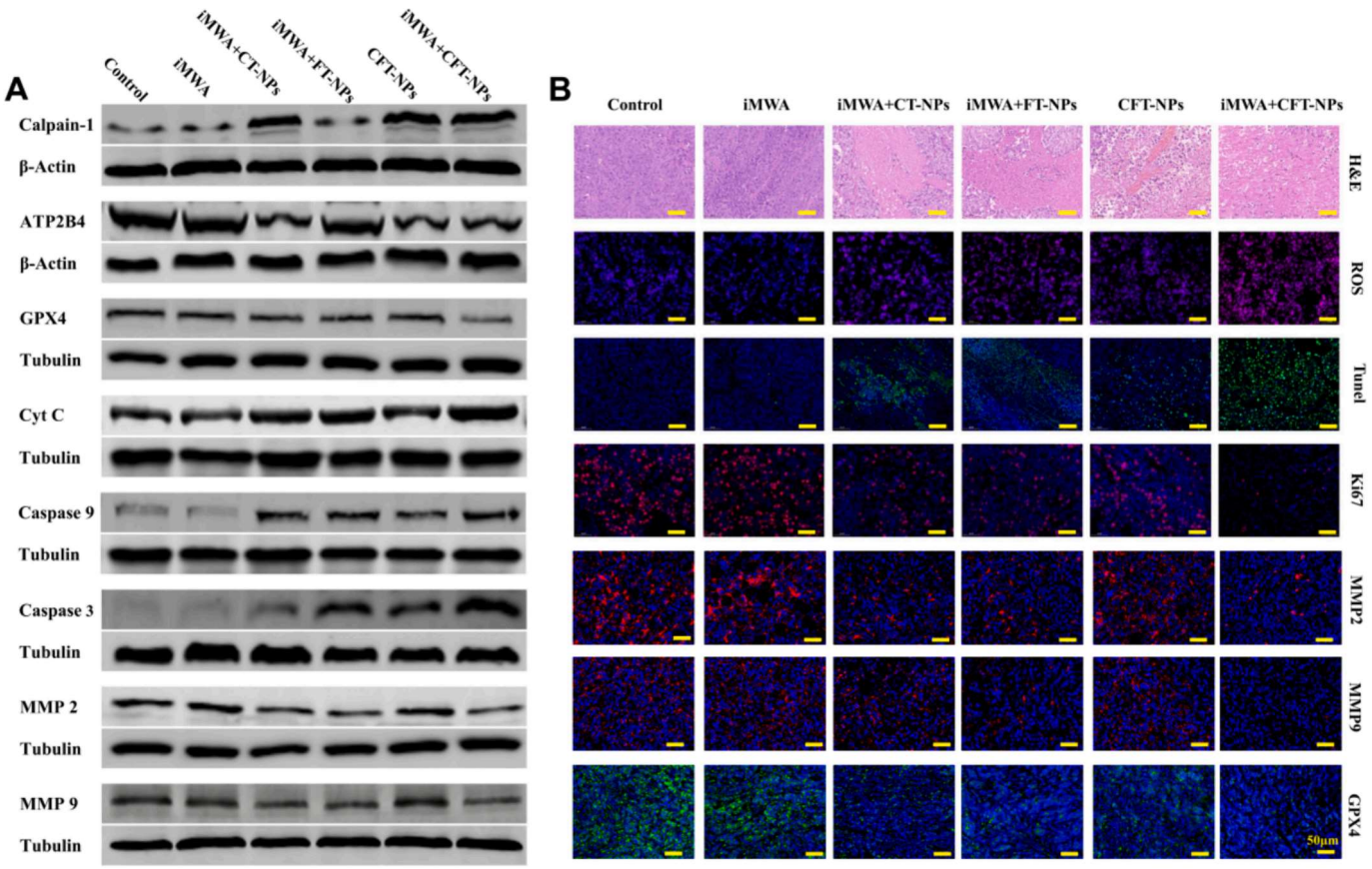


**Fig. 6.** (A) Western blot bands representing various proteins extracted from Hepa 1–6 tumors in different groups at the end of the experimental period; (B) staining images of H&E, ROS, Tunel, Ki67, MMP 2, MMP 9, and GPX 4 from tumor slices isolated from Hepa 1–6 tumor-bearing mice in different groups at the end of the experimental period.

were further supported by histological assessments, including H&E staining, Ki67 staining, and TUNEL staining of tumor slices (Fig. 6**B**). Specifically, H&E and TUNEL staining revealed extensive cellular nucleus damage in the iMWA + CFT-NPs group, indicating a higher rate of tumor cell apoptosis compared to other groups. Concurrently, Ki67 expression, a biomarker of cell proliferation, reached its lowest level in the iMWA + CFT-NPs group. These comprehensive results underscore the effectiveness of the $Fe^{2+}$ and $Ca^{2+}$ combination in augmenting the therapeutic benefits of iMWA.

### 3.6. *Ferroptosis and calcium overload synergistically contribute to tumor ablation*

To gain deeper molecular insights into the mechanism of tumor ablation, fresh tumor tissues were harvested for subsequent western blot analysis (Fig. 6**A,** Figure S25). Calpain-1 (μ-Calpain), a calcium-activated neutral cysteine protease, is activated by increased intracellular calcium concentrations that typically occur during apoptosis. ATP2B4 (ATPase Plasma Membrane $Ca^{2+}$ Transporting 4) functions to remove bivalent calcium ions from eukaryotic cells against steep concentration gradients, crucial for maintaining intracellular calcium homeostasis. Notably, a significant upregulation of Calpain-1 was observed in the iMWA + CT-NPs, CFT-NPs, and iMWA + CFT-NPs groups, while ATP2B4 expression displayed an inverse trend. This suggested that the $Ca^{2+}$ enrichment in the NPs indeed disrupts intracellular $Ca^{2+}$ homeostasis, leading to cell apoptosis.

Next, we delved into the crucial aspect of intracellular oxidative stress, focusing on ROS, a key marker. Consistent with our *in vitro* studies, ROS levels were upregulated within tumor tissue, attributed to ferroptosis triggered by the presence of $Fe^{2+}$ and the heating effect (Fig. 6**B**). Ferroptosis involved glutathione peroxidase 4 (GPX 4), which utilized reduced GSH to convert phospholipid hydroperoxides to lipid alcohols. Therefore, we evaluated the expression level of GPX 4. The results revealed a decrease in GPX 4 expression in the CFT-NPs group compared to the control, with the lowest level observed in the iMWA + CTF-NPs groups, indicative of the onset of ferroptosis (Fig. 6**A, B**). Furthermore, we examined the cell apoptosis signaling pathway. Notably, Cyt c expression significantly upregulated in the iMWA + CFT-NPs group. Cyt c plays a pivotal role in caspase activation, as various apoptotic stimuli trigger its release from mitochondria. This, in turn, initiates a cascade of biochemical reactions leading to caspase activation and subsequent cell death. This was corroborated by the marked upregulation of Caspase 3 and 9 production. Intriguingly, the expression of MMP 2 and MMP 9 protein were downregulated following iMWA + CFT-NPs treatment, demonstrating a reduced potential for tumor cell metastasis. Taken together, the as-prepared CFT-NPs showed immense promise in suppressing tumor growth and further metastasis. This is attributed to the high concentrations of $Ca^{2+}$ and $Fe^{2+}$, which, in synergy with hyperthermia, disrupt $Ca^{2+}$ homeostasis and induce cellular ferroptosis in tumor cells, ultimately leading to immunogenic cell death.

### 3.7. *In vivo long-term biocompatibility*

To assess the biocompatibility of iMWA + CFT-NPs, we monitored their *in vivo* toxicity. Following 21 days of treatment, the primary organs (spleen, lung, liver, kidney, and heart) were excised and further assays were performed via H&E staining. Notably, the results revealed no histopathological aberrations, such as necrosis, or alteration in the cellular architecture when compared to the control group (Fig. 7**A**). Moreover, we tracked blood biochemical and hematological parameters over time to evaluate the function of different organs (Fig. 7**B**). No significant differences were observed in the blood level of red blood cells (RBCs), platelets (PLT), or white blood cells (WBCs) compared to the control. Furthermore, biochemical markers such as alanine

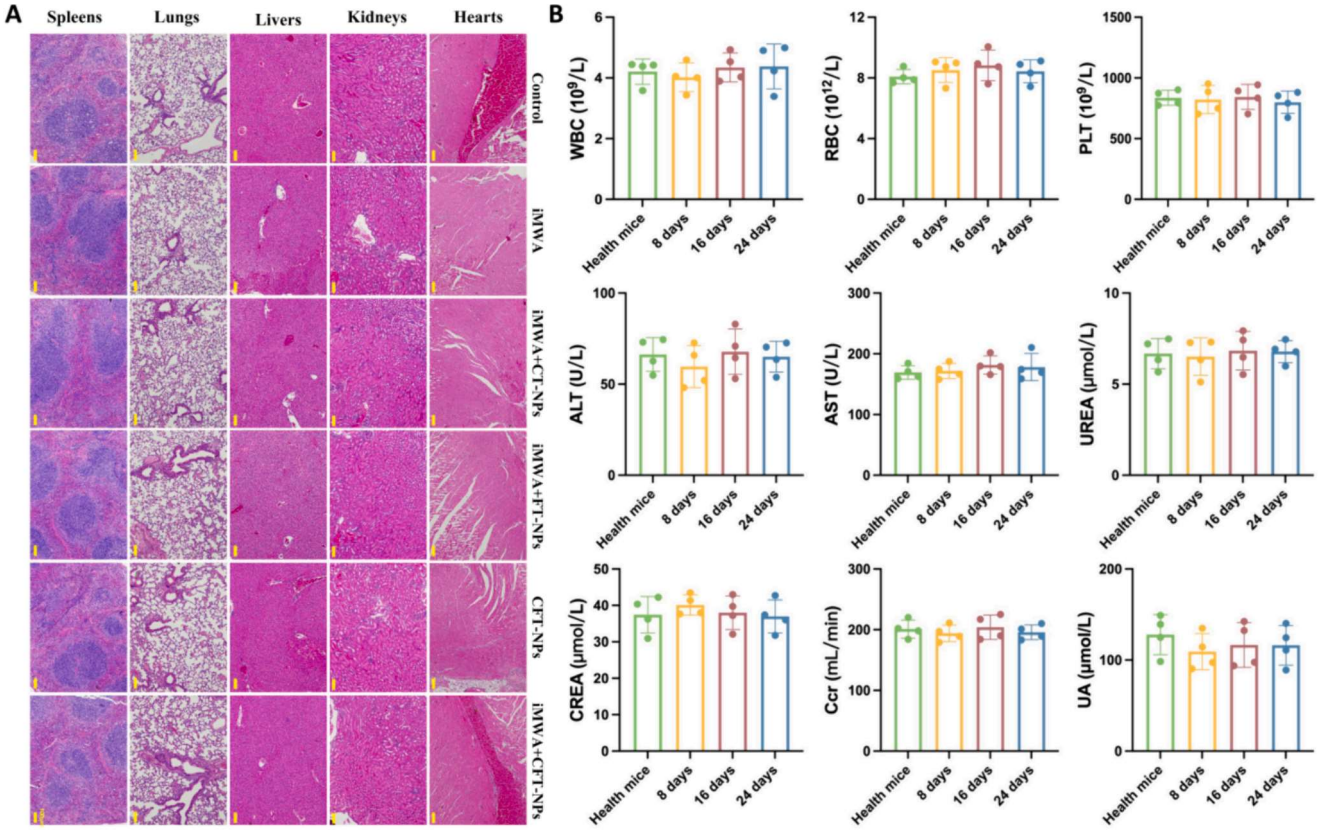


**Fig. 7.** (A) H&E microscopic images of major organs in different groups; (B) quantitative data of blood and biochemical indexes in both healthy mice and treated mice. Data are expressed as mean ± SD (n = 4). The significance analysis for inter-group statistical comparisons was conducted using ANOVA.

transaminase (ALT), aspartate transferase (AST), blood urea nitrogen (BUN), CREA, and uric acid (UA) remained unchanged, indicating the excellent biocompatibility of CFT-NPs in combination with iMWA. Overall, the iMWA + CFT-NPs treatment did not exhibit any notable adverse effects on the functionality of the tested organs in mice or induce metabolic abnormalities. These findings further strengthen the biocompatibility and safety profile of the iMWA + CFT-NPs treatment, supporting its potential for clinical development.

## 4. Conclusion

In summary, we have successfully crafted a novel bimetallic nanosensitizer that leverages the synergistic power of TA and iron/calcium dual metal ions. This innovative approach not only significantly boosts the efficacy of MWA but also disrupts cell homeostasis, thereby enhancing the antitumor efficacy of microwave technology in HCC treatment. The nanosensitizer, with its uniform nanosize, efficiently targets and delivers therapeutic agents to the tumor site, facilitating their internalization by HCC cells. Once inside the cells, the acidic microenvironment triggered the release of the bimetallic ions, leading to a cooperative enhancement in the conversion of low-frequency microwave electromagnetic energy into heat, resulting in improved tumor ablation. Simultaneously, the released TA reduced iron ions and reacted with hydrogen peroxide to generate ROS, ultimately inducing lipid oxidation and ferroptosis. Calcium ions, on the other hand, disrupt mitochondrial dysfunction, further promoting cell apoptosis. Both *in vivo* and *in vitro* studies demonstrated that dual-metal ions MWA nanosensitizer provided a significant inhibition of tumor growth and reduced the expression of matrix metalloproteinases (MMP 2 and MMP 9). This innovative approach offers a new paradigm for the design of MWA nanosensitizer, overcoming the limitations of iMWA and paving the way for potential clinical applications in HCC treatment.

## CRediT authorship contribution statement

**Guanhua Qiu:** Writing – original draft, Formal analysis. **Duo Wang:** Formal analysis, Conceptualization. **Peihan Xie:** Software, Methodology. **Zelun Li:** Data curation. **Niqiang Zhou:** Data curation. **Xiaoqian Zhang:** Validation, Investigation. **Xiaobo Wang:** Validation, Investigation. **Jiali Tang:** Validation, Investigation. **Jun Cao:** Project administration, Conceptualization. **Junjie Liu:** Funding acquisition. **Danke Su:** Supervision, Resources.

## Declaration of competing interest

The authors declare that they have no known competing financial interests or personal relationships that could have appeared to influence the work reported in this paper.

## Data availability

The data that support the findings of this study are available from the corresponding author upon reasonable request.

## Acknowledgment

This project was supported and granted by the National Natural Science Foundation of China Regional Project (82160341 and 82260345), Guangxi Natural Science Foundation Key Project (2022GXNSFDA035060), Guangxi Key R&D Plan (Guike AB22080066) and Postdoctoral Fellowship Program of CPSF (BX20230068).

## Appendix A. Supplementary data

Supplementary data to this article can be found online at https://doi.org/10.1016/j.cej.2024.153368.

## References

[1] W.S. Wu, X. Yan, S. Chen, Y.X. Du, J.L. Hu, Y. Song, Z.B. Zha, Y.J. Xu, B.Q. Cao, S. H. Xuan, et al., Minimally invasive delivery of percutaneous ablation agent via magnetic colloidal hydrogel injection for treatment of hepatocellular carcinoma, Adv. Mater. (2024) e2309770, https://doi.org/10.1002/adma.202309770.
[2] Z. Liu, X. Tan, Y. Huang, W. Li, N. Yang, R. Yuan, Q. Cheng, L. Liu, L. Ge, Microwave absorption-based magnetic liquid metal nano-missiles for thermodynamic/immunological cascade hepatoma therapy, Chem. Eng. J. (Lausanne, Switzerland) 2023 (471) (1996) 144688, https://doi.org/10.1016/j.cej.2023.144688.
[3] H. Pan, M. Yu, X. Tang, X. Mao, M. Liu, K. Zhang, C. Qian, J. Wang, H. Xie, W. Qiu, et al., Preoperative single-dose camrelizumab and/or microwave ablation in women with early-stage breast cancer: A window-of-opportunity trial, Med. (2024), https://doi.org/10.1016/j.medj.2024.01.015.
[4] L. Zheng, J.P. Dou, Z.Y. Han, F.Y. Liu, J. Yu, Z.G. Cheng, X.L. Yu, H. Wang, Z. B. Cong, S.R. Wang, et al., Microwave ablation for papillary thyroid microcarcinoma with and without US-detected capsule invasion: A multicenter prospective cohort study, Radiology 307 (2023) e220661, https://doi.org/10.1148/radiol.220661.
[5] S. Li, Z. Chen, L. Tan, Q. Wu, X. Ren, C. Fu, M. Niu, H. Li, X. Meng, MOF@COF nanocapsule for the enhanced microwave thermal-dynamic therapy and anti-angiogenesis of colorectal cancer, Biomaterials 283 (2022) 121472, https://doi.org/10.1016/j.biomaterials.2022.121472.
[6] D. Wang, M. Zhang, G. Qiu, C. Rong, X. Zhu, G. Qin, C. Kong, J. Zhou, X. Liang, Z. Bu, et al., Extracellular matrix viscosity reprogramming by in situ au bioreactor-boosted microwavegenetics disables tumor escape in CAR-T immunotherapy, ACS Nano 17 (2023) 5503–5516, https://doi.org/10.1021/acsnano.2c10845.
[7] Y. Shen, L. Chen, X. Guan, X. Han, X. Bo, S. Li, L. Sun, Y. Chen, W. Yue, H. Xu, Tailoring chemoimmunostimulant bioscaffolds for inhibiting tumor growth and metastasis after incomplete microwave ablation, ACS Nano 15 (2021) 20414–20429, https://doi.org/10.1021/acsnano.1c08826.
[8] Y. Zhi, Z. Yu, D. Zi, L. Wei, Y. Nai, W. Xian, F. Liang, L. Zhuang, Tumor-killing nanoreactors fueled by tumor debris can enhance radiofrequency ablation therapy and boost antitumor immune responses, Nat. Commun. 12 (1) (2021) 4299.
[9] A. Kalin, M. Hassan, M. Anderson, N. Rahman, Bilious pleuritis following transpulmonary radiofrequency ablation of liver metastases, Thorax 73 (2018) 493–494, https://doi.org/10.1136/thoraxjnl-2017-210508.
[10] P. Zhang, S. Yao, Y. Tang, S. Wan, X. Chen, L. Ma, A side-effect-free interventional therapy for precisely eliminating unresectable cancer pain, ACS Nano 17 (2023) 23535–23544, https://doi.org/10.1021/acsnano.3c06511.
[11] Q. Wu, N. Xia, D. Long, L. Tan, W. Rao, J. Yu, C. Fu, X. Ren, H. Li, L. Gou, et al., Dual-functional supernanoparticles with microwave dynamic therapy and microwave thermal therapy, Nano Lett. 19 (2019) 5277–5286, https://doi.org/10.1021/acs.nanolett.9b01735.
[12] C. Fu, H. Zhou, L. Tan, Z. Huang, Q. Wu, X. Ren, J. Ren, X. Meng, Microwave-activated Mn-doped zirconium metal-organic framework nanocubes for highly effective combination of microwave dynamic and thermal therapies against cancer, ACS Nano 12 (2018) 2201–2210, https://doi.org/10.1021/acsnano.7b08868.
[13] Y. Feng, Q. Chen, C. Jin, Y. Ruan, Q. Chen, W. Lin, C. Zhu, T. Zhang, Y. Zhang, J. Gao, et al., Microwave-activated Cu-doped zirconium metal-organic framework for a highly effective combination of microwave dynamic and thermal therapy, J. Control. Release 361 (2023) 102–114, https://doi.org/10.1016/j.jconrel.2023.07.046.
[14] X. Wang, M. He, Y. Zhao, J. He, J. Huang, L. Zhang, Z. Xu, Y. Kang, P. Xue, Bimetallic PtPd atomic clusters as apoptosis/ferroptosis inducers for antineoplastic therapy through heterogeneous catalytic processes, ACS Nano 18 (2024) 8083–8098, https://doi.org/10.1021/acsnano.3c11610.
[15] G. He, Y. Pan, F. Zeng, S. Qin, X. Luan, Q. Lu, C. Xie, P. Hu, Y. Gao, J. Yang, et al., Microfluidic synthesis of CuH nanoparticles for antitumor therapy through hydrogen-enhanced apoptosis and cuproptosis, ACS Nano 18 (2024) 9031–9042, https://doi.org/10.1021/acsnano.3c12796.
[16] Z. Wang, X. Wang, X. Dai, T. Xu, X. Qian, M. Chang, Y. Chen, Two-dimensional catalytic nanozyme enables cascade enzyodynamic effect-boosted and Ca(2+) overload-induced synergistic ferroptosis/apoptosis in tumor, Adv. Mater. (2024) e2312316, https://doi.org/10.1002/adma.202312316.
[17] D. Wang, M. Zhang, Y. Zhang, G. Qiu, J. Chen, X. Zhu, C. Kong, X. Lu, X. Liang, L. Duan, et al., Intraparticle double-scattering-decoded sonogenetics for augmenting immune checkpoint blockade and CAR-T therapy, Adv. Sci. (Weinh) 9 (2022) e2203106, https://doi.org/10.1002/advs.202203106.
[18] Z. Guo, X. Gao, J. Lu, Y. Li, Z. Jin, A. Fahad, N.U. Pambe, H. Ejima, X. Sun, X. Wang, et al., Apoptosis and paraptosis induced by disulfiram-loaded Ca(2+)/Cu (2+) dual-ions nano trap for breast cancer treatment, ACS Nano 18 (2024) 6975–6989, https://doi.org/10.1021/acsnano.3c10173.
[19] Y. Zhu, Z. Yang, Z. Pan, Y. Hao, C. Wang, Z. Dong, Q. Li, Y. Han, L. Tian, L. Feng, et al., Metallo-alginate hydrogel can potentiate microwave tumor ablation for synergistic cancer treatment, Sci. Adv. 8 (2022) o5285, https://doi.org/10.1126/sciadv.abo5285.
[20] J.P. Dou, Q. Wu, C.H. Fu, D.Y. Zhang, J. Yu, X.W. Meng, P. Liang, Amplified intracellular Ca(2+) for synergistic anti-tumor therapy of microwave ablation and chemotherapy, J. Nanobiotechnol. 17 (2019) 118, https://doi.org/10.1186/s12951-019-0549-0.
[21] F. Yang, J. Dong, Z. Li, Z. Wang, Metal-organic frameworks (MOF)-assisted sonodynamic therapy in anticancer applications, ACS Nano 17 (2023) 4102–4133, https://doi.org/10.1021/acsnano.2c10251.

[22] D. Wang, X. Zhu, X. Wang, Q. Wang, K. Yan, G. Zeng, G. Qiu, R. Jiao, X. Lin, J. Chen, et al., Multichannel sonocatalysis amplifiers target IDH1-mutated tumor plasticity and attenuate Ros tolerance to repress malignant cholangiocarcinoma, Adv. Funct. Mater. 33 (2023), https://doi.org/10.1002/adfm.202303869.
[23] L. Zhao, F. Chang, Y. Tong, J. Yin, J. Xu, H. Li, L. Du, Y. Jiang, A Multifunctional bimetallic nanoplatform for synergic local hyperthermia and chemotherapy targeting HER2-positive breast cancer, Adv. Sci. (Weinh) (2024) e2308316, https://doi.org/10.1002/advs.202308316.
[24] D. Jana, D. Wang, A.K. Bindra, Y. Guo, J. Liu, Y. Zhao, Ultrasmall alloy nanozyme for ultrasound- and near-infrared light-promoted tumor ablation, ACS Nano 15 (2021) 7774–7782, https://doi.org/10.1021/acsnano.1c01830.
[25] P. Zheng, B. Ding, G. Zhu, C. Li, J. Lin, Biodegradable Ca(2+) nanomodulators activate pyroptosis through mitochondrial Ca(2+) overload for cancer immunotherapy, Angew. Chem. Int. Ed. Engl. 61 (2022) e202204904, https://doi.org/10.1002/anie.202204904.
[26] C. Lin, C. Huang, Z. Shi, M. Ou, S. Sun, M. Yu, T. Chen, Y. Yi, X. Ji, F. Lv, et al., Biodegradable calcium sulfide-based nanomodulators for H (2)S-boosted Ca(2+)-involved synergistic cascade cancer therapy, Acta Pharm. Sin. B 12 (2022) 4472–4485, https://doi.org/10.1016/j.apsb.2022.08.008.
[27] G. Song, M. Li, S. Fan, M. Qin, B. Shao, W. Dai, H. Zhang, X. Wang, B. He, Q. Zhang, Boosting synergism of chemo- and immuno-therapies via switching paclitaxel-induced apoptosis to mevalonate metabolism-triggered ferroptosis by bisphosphonate coordination lipid nanogranules, Acta Pharm. Sin. B 14 (2024) 836–853, https://doi.org/10.1016/j.apsb.2023.08.029.
[28] Y. Ma, X. Zhao, P. Tian, K. Xu, J. Luo, H. Li, M. Yuan, X. Liu, Y. Zhong, P. Wei, et al., Laser-ignited lipid peroxidation nanoamplifiers for strengthening tumor photodynamic therapy through aggravating ferroptotic propagation and sustainable high immunogenicity, Small (2023) e2306402, https://doi.org/10.1002/smll.202306402.
[29] L. Yang, X. Wang, Y. Zhao, Y. Li, X. Wang, J. Deng, Z. Qi, Strengthened EPR effect of AIEgen-Poly(I:C) composite nanoparticles to facilitate antigen cross-presentation and improve melanoma prognosis by evoking immunity, Chem. Eng. J. 473 (2023) 145205, https://doi.org/10.1016/j.cej.2023.145205.
[30] J. Liu, J. Zhan, Y. Zhang, L. Huang, J. Yang, J. Feng, L. Ding, Z. Shen, X. Chen, Ultrathin clay nanoparticles-mediated mutual reinforcement of ferroptosis and cancer immunotherapy, Adv. Mater. 36 (2024) e2309562, https://doi.org/10.1002/adma.202309562.
[31] D. Wang, G. Qiu, X. Zhu, Q. Wang, C. Zhu, C. Fang, J. Liu, K. Zhang, Y. Liu, Macrophage-inherited exosome excise tumor immunosuppression to expedite immune-activated ferroptosis, J. Immunother. Cancer 11 (2023), https://doi.org/10.1136/jitc-2022-006516.
[32] P. Zheng, B. Ding, R. Shi, Z. Jiang, W. Xu, G. Li, J. Ding, X. Chen, A Multichannel Ca(2+) nanomodulator for multilevel mitochondrial destruction-mediated cancer therapy, Adv. Mater. 33 (2021) e2007426, https://doi.org/10.1002/adma.202007426.
[33] W. Bao, M. Liu, J. Meng, S. Liu, S. Wang, R. Jia, Y. Wang, G. Ma, W. Wei, Z. Tian, MOFs-based nanoagent enables dual mitochondrial damage in synergistic antitumor therapy via oxidative stress and calcium overload, Nat. Commun. 12 (2021) 6399, https://doi.org/10.1038/s41467-021-26655-4.
[34] X. Xie, Q. Lan, J. Zhao, S. Zhang, L. Liu, Y. Zhang, W. Xu, M. Shao, J. Peng, S. Xia, et al., Structure-based design of pan-coronavirus inhibitors targeting host cathepsin L and calpain-1, Signal Transduct. Target. Ther. 9 (2024) 54, https://doi.org/10.1038/s41392-024-01758-8.
[35] T. Prochnicki, M.B. Vasconcelos, K.S. Robinson, M. Mangan, D. De Graaf, K. Shkarina, M. Lovotti, L. Standke, R. Kaiser, R. Stahl, et al., Mitochondrial damage activates the NLRP10 inflammasome, Nat. Immunol. 24 (2023) 595–603, https://doi.org/10.1038/s41590-023-01451-y.
[36] L.W. Wang, H. Shen, L. Nobre, I. Ersing, J.A. Paulo, S. Trudeau, Z. Wang, N. A. Smith, Y. Ma, B. Reinstadler, et al., Epstein-barr-virus-induced one-carbon metabolism drives B cell transformation, Cell Metab. 30 (2019) 539–555, https://doi.org/10.1016/j.cmet.2019.06.003.
[37] H. Zhang, M. Cui, D. Tang, B. Wang, G. Liang, C. Xu, H. Xiao, Localization of cancer cells for subsequent robust photodynamic therapy by ROS responsive polymeric nanoparticles with anti-metastasis complexes NAMI-A, Adv. Mater. (2023) e2310298, https://doi.org/10.1002/adma.202310298.
[38] N. Amaly, A.Y. EL-Moghazy, N. Nitin, G. Sun, P.K. Pandey, Synergistic adsorption-photocatalytic degradation of tetracycline by microcrystalline cellulose composite aerogel dopped with montmorillonite hosted methylene blue, Chem. Eng. J. (Lausanne, Switzerland) 2022 (430) (1996) 133077, https://doi.org/10.1016/j.cej.2021.133077.
[39] S. Tian, H. Man, L. Jun, L. Shui, Y. Peng, Y. Jian, C. Yu, Z. Sheng, X. Li, P. Zhen, et al., Insufficient radiofrequency ablation promotes hepatocellular carcinoma metastasis through N6-methyladenosine mRNA methylation-dependent mechanism, Hepatology 74 (3) (2021) 1339–1356, https://doi.org/10.1002/hep.31766.
[40] F. Tian, S. Wang, K. Shi, X. Zhong, Y. Gu, Y. Fan, Y. Zhang, M. Yang, Dual-depletion of intratumoral lactate and ATP with radicals generation for cascade metabolic-chemodynamic therapy, Adv. Sci. (Weinh) 8 (2021) e2102595, https://doi.org/10.1002/advs.202102595.
[41] Z. Wang, Y. Guo, Y. Fan, J. Chen, H. Wang, M. Shen, X. Shi, Metal-phenolic-network-coated dendrimer-drug conjugates for tumor MR imaging and chemo/chemodynamic therapy via amplification of endoplasmic reticulum stress, Adv. Mater. 34 (2022) e2107009, https://doi.org/10.1002/adma.202107009.
[42] L. Li, Z. Yang, W. Fan, L. He, C. Cui, J. Zou, W. Tang, O. Jacobson, Z. Wang, G. Niu, et al., In situ polymerized hollow mesoporous organosilica biocatalysis nanoreactor for enhancing ROS-mediated anticancer therapy, Adv. Funct. Mater. 30 (2020), https://doi.org/10.1002/adfm.201907716.
[43] N. Liu, Q. Lin, Z. Huang, C. Liu, J. Qin, Y. Yu, W. Chen, J. Zhang, M. Jiang, X. Gao, et al., Mitochondria-targeted prodrug nanoassemblies for efficient ferroptosis-based therapy via devastating ferroptosis defense systems, ACS Nano 18 (2024) 7945–7958, https://doi.org/10.1021/acsnano.3c10133.
[44] X. Bian, N. Fan, M. Li, D. Han, J. Li, L. Fan, X. Li, L. Kong, H. Tang, S. Ding, et al., An ER-horse detonating stress cascade for hepatocellular carcinoma nanotherapy, ACS Nano 17 (2023) 4896–4912, https://doi.org/10.1021/acsnano.2c11922.
[45] E.C. Cheung, K.H. Vousden, The role of ROS in tumor development and progression, Nat. Rev. Cancer 22 (2022) 280–297, https://doi.org/10.1038/s41568-021-00435-0.